Granular Collapses

Joshua Sam Caplan
Trinity College
University of Cambridge

July 2018

This dissertation is submitted for the degree of Master of Science

This dissertation is the result of my own work and includes nothing which is the outcome of work done in collaboration except as declared in the Preface and specified in the text.

It is not substantially the same as any that I have submitted, or, is being concurrently submitted for a degree or diploma or other qualification at the University of Cambridge or any other University or similar institution except as declared in the Preface and specified in the text. I further state that no substantial part of my dissertation has already been submitted, or, is being concurrently submitted for any such degree, diploma or other qualification at the University of Cambridge or any other University or similar institution except as declared in the Preface and specified in the text.

Granular Collapses

Joshua Sam Caplan

Abstract

The research presented in this thesis concerns the granular collapse problem, where a mass of a granular material is allowed to collapse under its own weight and spread out across a base surface. Whilst this collapse process has been studied in the past, there are a number of potentially important aspects of this problem that have not been fully considered. We start this thesis by repeating previous experiments with the simplest case of a cylindrical mass of a monodisperse material of approximately spherical grains flowing over a horizontal base. By applying new measurement techniques we find differences with previously reported results. We then extend the problem to the bidisperse case by using layers of two types of particles that differ only in their size. We find that, contrary to expectation, there is little segregation of the two species during the collapse. We then return to the monodisperse problem and consider the effects of increasing the initial column aspect ratio beyond the values previously considered. We first use an asymptotic analysis of the possible shapes of the final deposit to find restrictions on the large aspect ratio behaviour of the deposit's maximum height and radius. Finally, we perform monodisperse collapses of a range of materials with aspect ratios of up to 80. We find that the dynamics of the flow and the shape of the final deposit are significantly different in this regime.

Contents

1 Introduction **1**

1.1 Introduction to granular media 1
1.2 Problem description 2
1.3 Outline 3

2 Granular collapses **5**

2.1 Previous work 5
2.1.1 Monodisperse axisymmetric collapses 5
2.1.2 Other monodisperse experiments 10
2.1.3 Theoretical and numerical work 11
2.2 Experiments 13
2.3 Results 15
2.4 Vertically split columns 29
2.5 Discussion 31

3 Bidisperse collapses **35**

3.1 Segregation 35
3.2 Previous work 36
3.3 Experiments 38
3.4 Results 39
3.4.1 Flow dynamics 39
3.4.2 Final deposit 48
3.5 Different species ratios 51
3.6 Mixed columns 54

3.7 Discussion 58

4 Very high aspect ratio collapses **59**
4.1 Motivation 59
4.2 Large aspect ratio asymptotics 59
4.2.1 Discussion 63
4.2.2 Two dimensions 65
4.3 Experiments 66
4.3.1 Experimental set-up 66
4.3.2 Glass beads 67
4.3.3 Sand 78
4.3.4 Silicon carbide 81
4.4 Even higher aspect ratios 85
4.5 Discussion 89

5 Conclusions **91**
5.1 Summary 91
5.2 Open questions 92

Bibliography **95**

1 Introduction

1.1 Introduction to granular media

One of the key problems with understanding granular materials is the range of behaviours present in even a simple flow. In regions of low particle density granular materials can behave like a gas, with particles interacting almost exclusively through binary collisions. Unlike in gases however, these collisions are inelastic leading to major differences in behaviour. On the other hand, dense regions with little shear stress can behave like solids, with particles that are either stationary or creep slowly. If too high a stress is applied, however, the material can suddenly fail and begin flowing.

Between these two extremes granular materials exhibit fluid-like behaviour. This region is characterised by particles being in constant contact with each other but are still able to flow past each other. This leads to complex behaviour that is very different to more well known types of fluid.

This combination of behaviours means that flows of granular materials are notoriously difficult to model. In practice two main approaches are used: discrete element methods (DEM) and continuum models.

DEM take the simplest approach by modelling each individual particle and the collisions between them. The equations used to describe these are simple to derive and solve. For dense flows with almost constant collisions, this approach requires extremely small time steps to resolve every collision and makes DEM methods computationally expensive. As a result, the number of particles that can be modelled is limited and so the scale

of problems that can be considered is restricted.

Continuum models aim to avoid this by using a continuum approximation. The main difficulty is finding a suitable constitutive law for a granular material. The most successful law to date is the so-called $\mu(I)$ rheology. This approach is based on the observation by GDR MiDi (2004) that coefficient of friction μ depends on the *inertial number*

$$I = \frac{\dot{\gamma} d}{\sqrt{P/\rho}}, \tag{1.1}$$

where $\dot{\gamma}$ is the shear rate, d the particle diameter, P the pressure, and ρ the density of the particle. This was extended into a full rheology by Jop *et al.* (2005) and Jop *et al.* (2006).

In order to avoid deriving a full rheology we can instead depth-average the system as first done by Savage & Hutter (1989). For many flows we can make a long-wave assumption to end up with equations that resemble the shallow-water equations of classical fluid mechanics. The key advantage of this approach is that the complexity of rheology is removed.

1.2 Problem description

Avalanches and rockslides are real life examples of granular flows forming a significant hazard to people and structures. Both cases feature large amounts of granular material collapsing under its own weight and then spreading outwards. In order to protect communities at risk from such hazards much work has been put into designing systems to prevent, divert and halt such flows. For these to be most effective we need a better understanding of how granular materials behave then we currently have.

As these real life collapses are extremely complex, we will instead consider the simplified problem illustrated in figure 1.1. We fill a cylindrical

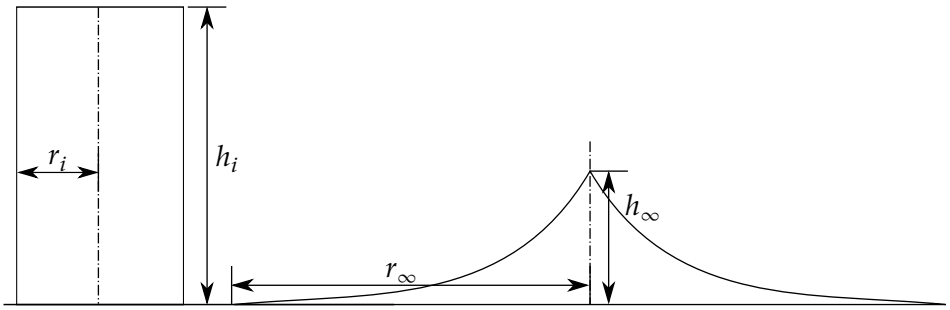

Figure 1.1: Illustration of basic axisymmetric column collapse problem.

tube of radius r_i with a granular material (or some combination of granular materials) to a height h_i. The cylinder is then quickly removed, allowing the material to spread across a horizontal base, forming a deposit of radius r_∞ and central height h_∞.

By considering the simplified problem we are able to perform laboratory scale experiments. The simplifications also allow the problem to be studied analytically and numerically, whereas a full-scale geophysical collapse might prove intractable. Our results could also be used to develop and verify models that can then be extended to real world problems.

1.3 Outline

We first consider the monodisperse granular collapse problem in chapter 2 by performing a series of experiments. We then repeat the experiments with bidisperse collapses in chapter 3. In chapter 4 we return to the monodisperse case but now consider significantly higher aspect ratio collapses through a simple geometric analysis and some basic experiment. Finally we discuss the results of this work in chapter 5.

2 Granular collapses

We begin by considering the case of monodisperse collapses. These have been extensively studied in the past and so allow us to verify our experimental set-up and techniques. These experiments also allow us to investigate some of the differences between previous work into these sort of collapses.

2.1 Previous work

2.1.1 Monodisperse axisymmetric collapses

The granular collapse problem was first considered by Lube *et al.* (2004) and Lajeunesse *et al.* (2004), who independently considered the collapse of a monodisperse cylindrical column. Both groups varied the initial column height and radius, the granular material used, and the choice of base material. Later work by Roche *et al.* (2011) and Warnett *et al.* (2013) produced broadly similar results. All four papers identified the initial aspect ratio,

$$a \equiv \frac{h_i}{r_i}, \tag{2.1}$$

as the key parameter in the collapse, with different regimes depending on its value.

Below a critical value, a_0, a circular, inwards moving front quickly appears on the top surface of column, separating a static inner region from

an outer slumping region. For the smallest aspect ratios this front never reaches the centre of the column, leaving a frustoconical (truncated cone) deposit with $h_\infty = h_i$. For larger values of a, the whole of the top surface is disturbed, giving a conical deposit with $h_\infty < h_i$.

When the column aspect ratio is above the critical value, $a > a_0$, the dynamics are very different. The top region falls vertically downwards whilst retaining its shape. As the top of the column approaches the base, it deforms to form a dome, which, in turn, collapses to give a central conical region. Whilst this is ongoing, the column spreads axisymmetrically outwards, quickly reaching a maximum speed, which it maintains until almost the end of the collapse. As the collapse finishes, a front separating a central static region from the flowing exterior appears and moves outwards until it reaches the edge of the collapse and the flow stops. The final deposit typically comprises a steep central cone surrounded by a thin, flat outer region, which Lajeunesse *et al.* (2004) refer to as a "Mexican hat" profile. In addition, for the largest aspect ratio collapses, Lube *et al.* (2004) found concentric bulges at the deposit edge and at half the run-out distance.

Roche *et al.* (2011) also identified an additional regime whose onset depends on the size of particles. This regime is characterised by the formation of a wave at the flow surface which spreads outwards. The wave moves faster than the flow front and overtakes it, causing the front to briefly accelerate before decelerating again. The final deposit comprises a central cone surrounded by a high circular ridge approximately half way between the deposit edge and the cone. For "coarse" particles (diameter 330 μm) this regime begins at $a \gtrsim 7$ and the deposit stops after the wave reaches the flow front. For "fine" particles (diameter 75 μm) this regime starts at $a \gtrsim 4$ but multiple waves form as the aspect ratio increases, up to a maximum of 5, with each wave overtaking its predecessor. The final deposit has a rippled surface from later small flows and up to three

concentric ridges form at higher aspect ratios. At the largest aspect ratios $a \gtrsim 18$ the deposits become asymmetric with diffuse edges.

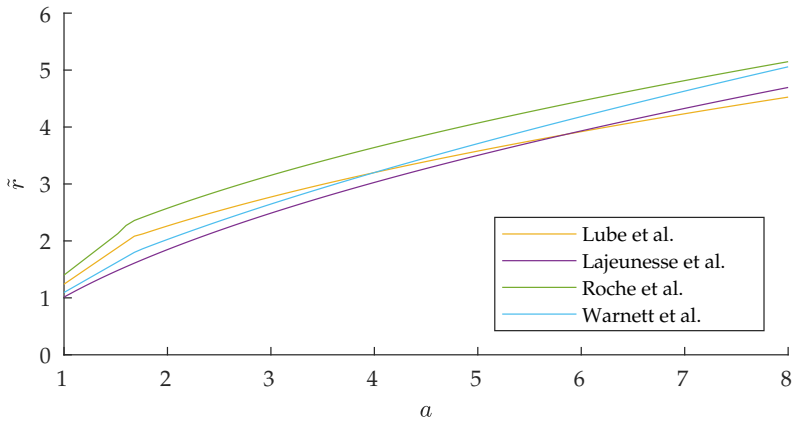

Figure 2.1: Graph of previously proposed laws (see equations (2.3) to (2.6)) for the non-dimensional run-out distance for a monodisperse, axisymmetric granular collapse.

All four papers proposed laws for the non-dimensional run-out distance

$$\tilde{r} \equiv \frac{r_\infty - r_i}{r_i}\,, \tag{2.2}$$

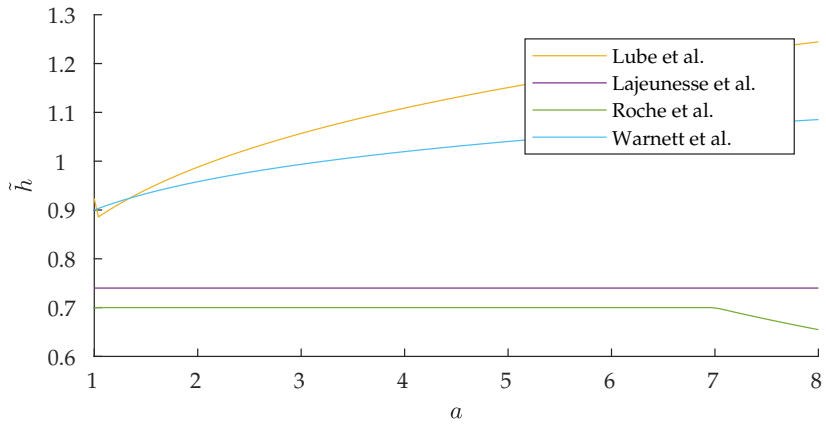

Figure 2.2: Graph of previously proposed laws (see equations (2.8) to (2.11)) for the non-dimensional central height for a monodisperse, axisymmetric granular collapse.

as a function of the initial aspect ratio, with

$$\tilde{r}_{lube} = \begin{cases} 1.24a & a < 1.7 \\ 1.6a^{1/2} & 1.7 < a < 10 \end{cases} \quad \text{(Lube } et\ al.\text{, 2004)}, \tag{2.3}$$

$$\tilde{r}_{lajeunesse} = \begin{cases} \frac{1}{2\mu_r}\left(a + \sqrt{4\mu_r^2 - \frac{a^2}{3}}\right) - 1 & a < 0.74 \\ \sqrt{\frac{3a}{0.74}} - 1 & a > 0.74 \end{cases} \quad \text{(Lajeunesse } et\ al.\text{, 2004)}, \tag{2.4}$$

$$\tilde{r}_{warnett} = \begin{cases} P_1 a + Q & a < 1.7 \\ P_2 a^{0.66} & a > 1.7 \end{cases} \quad \text{(Warnett } et\ al.\text{, 2013)}, \tag{2.5}$$

$$\tilde{r}_{roche} = \begin{cases} 1.4a & a < 1.6 \\ 1.82a^{1/2} & a > 1.6 \end{cases} \quad \text{(Roche } et\ al.\text{, 2011)}, \tag{2.6}$$

where μ_r is the coefficient of friction of the material, and P_1, P_2 and Q are functions of the initial radius. The law for Roche *et al.* (2011) is for their coarse particles as these are most similar in size to those used in the other papers. These sets of laws are, however, similar over the range of aspect ratios considered, as can be seen in figure 2.1. All four papers also proposed that the final, non-dimensional, central height of the deposit

$$\tilde{h} \equiv \frac{h_\infty}{h_i} \,, \tag{2.7}$$

followed power laws, but with significant disagreement about the behaviour at larger aspect ratios

$$\tilde{h}_{lube} = \begin{cases} a & a < 1 \\ 0.88a^{1/6} & 1.7 < a < 10 \end{cases} \quad \text{(Lube } et\ al.\text{, 2004)}, \tag{2.8}$$

$$\tilde{h}_{lajeunesse} = \begin{cases} a & a < 0.74 \\ 0.74 & a > 0.74 \end{cases} \quad \text{(Lajeunesse } et\ al.\text{, 2004)}, \tag{2.9}$$

$$\tilde{h}_{warnett} = \begin{cases} a & a < 0.9 \\ 0.90a^{0.09} & a > 0.9 \end{cases} \quad \text{(Warnett } et\ al.\text{, 2013)}, \tag{2.10}$$

$$\tilde{h}_{roche} = \begin{cases} a & a < 0.7 \\ 0.7 & 0.7 < a < 7 \\ ka^{-1/2} & \end{cases} \quad \text{(Roche } et\ al.\text{, 2011)}, \tag{2.11}$$

where k is a constant. Again the law for Roche *et al.* (2011) is for their coarse particles.

These laws are plotted in figure 2.2. Lube *et al.* (2004) found that neither the choice of granular material nor the choice of base had any effect on these laws. They also did not suggest a law for the transition region $1 < a < 1.7$. In contrast Lajeunesse *et al.* (2004) found that collapses over

smooth surfaces had the same run-out distance as those over rough surfaces but had a lower maximum height and thicker deposit edges. They also found that collapses with larger beads exhibited the same changes, which may be because the base roughness scale is less when compared to the size of the larger the beads.

2.1.2 Other monodisperse experiments

The granular collapse problem has also been extended to other geometries, most significantly to the quasi-two-dimensional equivalent, where a cuboidal column is allowed to collapse along a rectangular channel. The main experimental work on this topic was done by Balmforth & Kerswell (2005), Lajeunesse *et al.* (2005) and Lube *et al.* (2005), although Siavoshi & Kudrolli (2005) considered the problem earlier but in less detail. As with the axisymmetric problem, the key parameter is the initial aspect ratio with a critical value separating two main regimes. The run-out distances and final heights also follow power laws in the initial aspect ratio, with the exponents being dependent on the channel width. Notably, Balmforth & Kerswell (2005) found that, in contrast to the three-dimensional experiments, the collapses do depend on the material's frictional properties, with the rougher particles forming taller deposits with a shorter run-out. The exponents in the power laws, however, were not affected.

In addition, a variety of other variations have be considered including collapses on slopes (e.g. Hogg, 2007), collapses immersed in a fluid (e.g. Meruane *et al.*, 2010), collapses on a rotating base (Warnett, 2014) and collapses with extremely non-spherical particles (Trepanier & Franklin, 2010).

2.1.3 Theoretical and numerical work

As well as the experimental work discussed above, there have been attempts to model the granular collapse problem numerically. Due to the complexities of modelling granular media, these typically work with the two- or quasi-two-dimensional problem, rather than the full axisymmetric system. Both DEM and continuum models have been used to study granular collapses.

The first DEM simulations were performed by Zenit (2005) who modelled a two-dimensional collapse and found similar results to the later experimental work of Lajeunesse *et al.* (2005) and Lube *et al.* (2005). Staron & Hinch (2005) performed similar modelling and identified the sideways ejection of mass as the falling column hits the base as a key factor in the collapse dynamics. They suggested that this is why simple shallow-water-like models fail at high aspect ratios. Like Balmforth & Kerswell (2005), Staron & Hinch (2006) found that the frictional properties mattered in their two-dimensional DEM simulations.

Kerswell (2005) was the first to study a continuum collapse model and considered a shallow-water-like model (similar to that first proposed by Savage & Hutter (1989)). The resulting system of equations can then be solved analytically in two dimensions using characteristics, but its axisymmetric equivalent must be solved numerically. They found that equations significantly overestimate the run-out distance due to neglecting the finite size of real grains and due to problems with the friction law used. They do, however, predict the linear trend in run-out at low aspect ratios. The model also predicts that h_∞ tends to a constant value for large aspect ratios, matching the observations of Lajeunesse *et al.* (2004). Similar results were independently found in the numerical work of Mangeney-Castelnau *et al.* (2005).

In an attempt to fix the deficiencies of of these simple models, Larrieu

et al. (2006) instead modelled the falling column as a flux of material at the centre, rather than as a physical column. This allowed them to reproduce the experimental run-out distances for $a < 10$ but required unrealistically large coefficients of friction. For larger aspect ratios they found that their model broke down due to the formation a temporary high central peak. They attribute this to the shallow-water equations only allowing material to move through surface slopes, limiting the rate at which material can accelerate horizontally. At higher aspect ratios the mass flux is too much for this acceleration and so material accumulates at the centre of the deposit.

The model was then further extended by Doyle *et al.* (2007) who added a static base layer and allowed the deposition of particles as the flow progressed. As a result they were able to reproduce the experimental scalings whilst using a realistic value for the coefficient of friction.

Mangeney *et al.* (2007) investigated the reasons why shallow-water-like models fail at high aspect ratios. They argued that the assumption of hydrostatic pressure within the column is the major cause of the failure of the models to match experiments. They also found that other effects like the neglect of vertical velocities are of lesser importance and the associated inaccuracies do not increase with aspect ratio.

Whilst shallow-water models have been the target of much work, far less research has been done into modelling collapses with a non-depth-integrated rheology. Early work into this was done by Lacaze & Kerswell (2009), who compared the stresses and strain rates from two-dimensional DEM simulations with the predictions of the $\mu(I)$ rheology, finding a good agreement. Lagrée *et al.* (2011) then used the rheology to model full two-dimensional collapses. They managed to reproduce the scalings seen in experiment but had problems modelling the flow front. In this region the model predicts large values for the inertial number that are outside the regime where the $\mu(I)$ rheology was established (GDR MiDi, 2004). Furthermore, in experiments the flow front comprises a cloud of bouncing

grains and the continuum approximation required by the $\mu(I)$ rheology becomes questionable. In addition Crosta *et al.* (2009) modelled 2D collapses using an elastoplastic rheology, again with good agreement with experimental results.

The work of Lagrée *et al.* (2011) was then extended into three dimensions by Riber (2017), who reproduced the main features of the experimental results. One notable difference is that they found that the run-out distance depended on initial height separately from the aspect ratio, with taller columns travelling further.

Alternative continuum approaches have also been considered. For example, Chen *et al.* (2012) developed a smoothed particle hydrodynamics based model and found good agreement with both quasi-two-dimensional and the three-dimensional collapse experiments. Mast *et al.* (2014) instead used a material point method to model two-dimensional collapses and also found a good agreement with experiments.

2.2 Experiments

A photograph of the experimental apparatus can be seen in figure 2.3. An acrylic cylinder with an internal radius of 32 mm was filled to a height h_i with spherical glass beads by pouring them through a funnel. Two different types of bead were used in these experiments: small, colourless beads with radii between 300 μm and 425 μm; and large, red beads with radii between 1000 μm and 1300 μm. To give their colour the red beads were manufactured with a coating but this did not not noticeably affect their properties compared with the uncoated colourless beads. These two species were chosen as they readily segregate in, for example, chute flows.

For each species, the total mass of material was varied from 200 g to 1200 g, giving initial heights between 40 mm and 255 mm, and initial as-

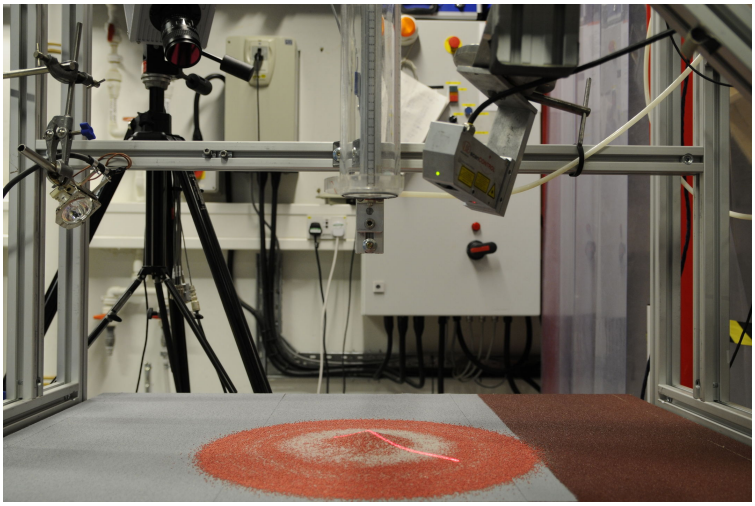

Figure 2.3: Photograph of the experimental apparatus. The high-speed camera can be seen in the top left of the image. The laser profile scanner is the metal box with the green light to the right of the cylinder. The red line on the deposit is from the laser scanner.

pect ratios between 1.3 and 8.0. To initiate the experiment, a pneumatic piston was used to lift the cylinder at a speed of approximately $0.7\,\mathrm{m\,s^{-1}}$, giving a repeatable start to the collapse. The column was then allowed to collapse over a horizontal base covered with sandpaper with an approximate roughness scale of $425\,\mu\mathrm{m}$. The sandpaper was chosen to prevent the particles, particularly the larger ones, from simply rolling outwards rather than forming a clear deposit.

The collapses were filmed using a high-speed camera (Photron FASTCAM SA 1.1) operating at 1000 frames per second. We can then use particle image velocimetry (PIV) to calculate the velocity at the surface of the flow. We used the DigiFlow software package (Dalziel, 2006) to perform the PIV which performs the calculations using a derivative of the synthetic Schlieren technique described in Dalziel *et al.* (2000). Unlike in with PIV

in fluids, we use the natural texture of the particles and do not need to introduce tracers.

We also used a laser profile scanner to record the radial height profiles of the central region during the collapse at a rate of 100 profiles per second. The laser used can be seen as the red line in figure 2.3 and is also visible in images from the high-speed camera.

In order to measure the radial spreading of the deposit, we initially trialled a method whereby the collapse was filmed from the side and the deposit width calculated from the images. However, the roughness of the base meant that the thin edge of the deposit could not be seen, resulting in the measured radii being significantly underestimated. Instead we filmed the deposit from above and used a computer program to correct for perspective and find the circle that best fitted the deposit edge. This method allowed us to obtain high precision measurements of the radius throughout the collapse.

One issue with any measurement of the deposit radius is that deposit edge is ambiguous, with the bulk of the deposit surrounded by a diffuse ring of individual grains. As we are interested in the bulk flow of granular material—as opposed to the motion of individual grains—our measurements consider only those particles that are in contact with the central deposit. This choice neglects only a small amount ($<1\%$ by mass) of material and is the intuitive definition of the deposit edge.

2.3 Results

Figure 2.4 shows typical example collapses for both materials. Initially the material falls straight downwards before spreading axisymmetrically outwards across the base. Eventually the collapse stops with some particles on the edge escaping from the main deposit and leaving a dilute ring of

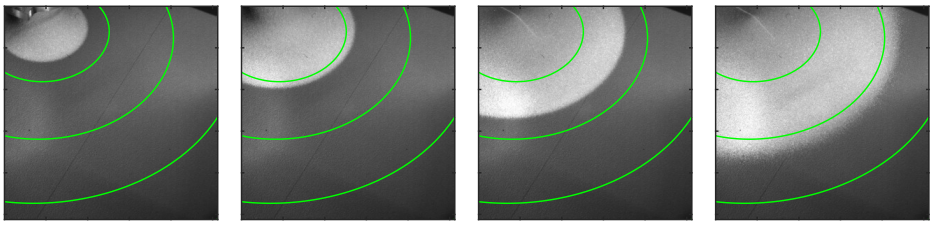

(a) Small particles ($a = 8.0$)

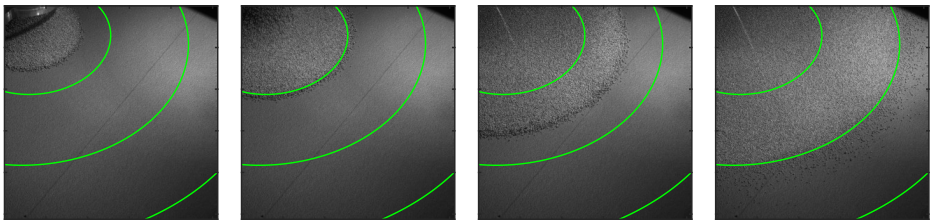

(b) Large particles ($a = 7.9$)

Figure 2.4: Images of column collapses of different sizes of glass beads. Images are taken 200 ms, 300 ms, 400 ms and 600 ms after the start of the collapse. Green arcs are at 100 mm intervals.

particles. This is less visible for the smaller particles due to them being too small to be clearly seen. Smaller aspect ratio collapses behave similarly within the range we considered, with the main difference being that they stop sooner.

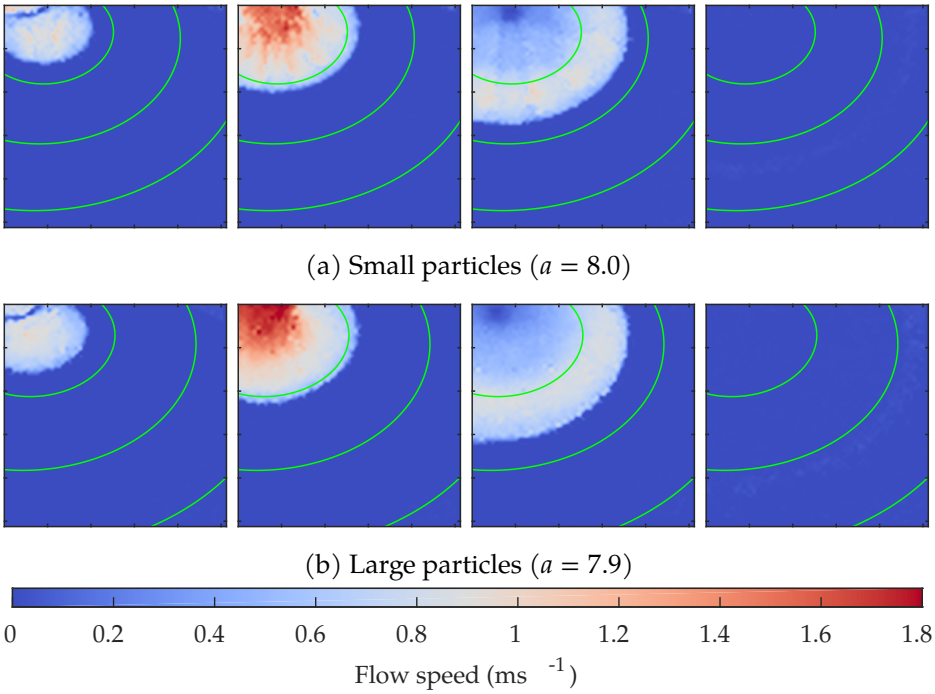

(a) Small particles ($a = 8.0$)

(b) Large particles ($a = 7.9$)

Figure 2.5: Flow speeds for column collapses of different types. Images are taken 200 ms, 300 ms, 400 ms and 600 ms after the start of the collapse. Collapses are the same as in figure 2.4. Green arcs are at 100 mm intervals.

Figure 2.5 shows the flow speed for the same collapses and at the same times as in figure 2.4. Initially the retracting cylinder obstructs the camera resulting in an anomalous region of "zero" velocity. As the collapses continues the flow accelerates with its maximum velocity at the centre of the deposit. The oblique angle of the camera means that we also pick up

a component of the downwards velocity of the collapsing column, leading to inaccurate measurements at the centre, where this is greatest, and a spurious asymmetry. As the collapse continues it first stops at the centre before finally coming to a complete stop.

Figures 2.6 and 2.7 illustrate the dynamics better by showing time series of the raw video data for a range of collapses, with each horizontal line showing the image captured along a specific radial line and with time progressing upwards. The choice of line is irrelevant in this case as the flow is axisymmetric. This process causes radial moving features of the data to appear as lines in the time series. The angle of a line then shows the speed of the feature, with vertical lines representing stationary features (e.g. the base) and shallower lines representing fast moving features (e.g. the deposit edge).

Initially we see the cylinder retract and the deposit begin spreading outwards. Although the cylinder base partially blocks this region, we can see that the deposit edge rapidly accelerates before the rate of acceleration suddenly slows. The flow then continues to spread at a slowly increasing speed until the end of the collapse at which point it quickly decelerates to a stop.

For the smallest aspect ratios considered, the collapse first stops at the edge of the deposits. A stopped region then spreads inwards and the whole deposit stops almost instantaneously. For the larger collapses, we instead see that the flow first stops at the centre. In these cases the region of stopped material then spreads outwards until it hits the flow front and all motion stops. As this region approaches the edge of the deposit, the edge rapidly decelerates apart from a few particles that slide away from the main deposit. These are most clearly visible in figure 2.7e but are also present in all collapses of either particle type.

One significant feature is that the time series for each material are all the same at early times. As the collapses proceed they only start to differ once

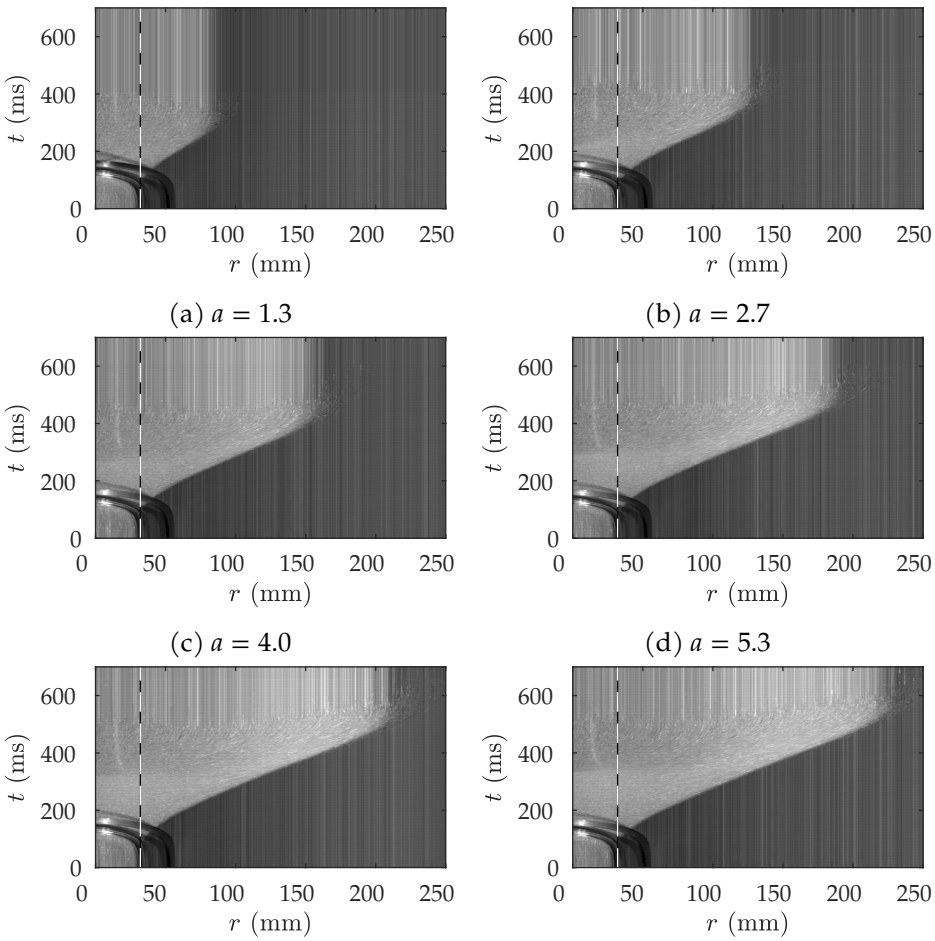

(a) $a = 1.3$ (b) $a = 2.7$

(c) $a = 4.0$ (d) $a = 5.3$

(e) $a = 6.6$ (f) $a = 8.0$

Figure 2.6: Video time series of collapses of small particles. The black and white line at 32 mm marks the initial radius of the column.

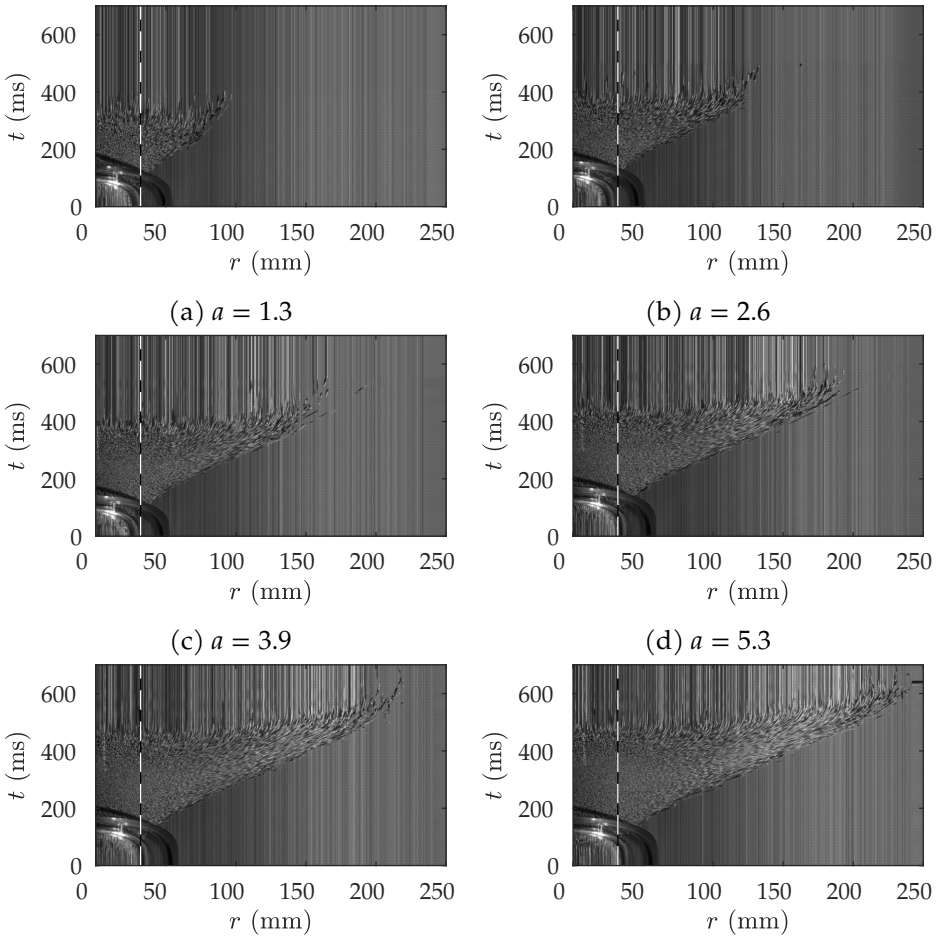

(a) $a = 1.3$ (b) $a = 2.6$

(c) $a = 3.9$ (d) $a = 5.3$

(e) $a = 6.6$ (f) $a = 7.9$

Figure 2.7: Video time series of collapses of large particles. The black and white line at 32 mm marks the initial radius of the column.

the column has finished collapsing, at which point each collapse stops in the same manner. This suggests that, from the point of view of the spreading process, the falling column acts primarily as a source of material and energy (compare the "rain" of Larrieu *et al.* (2006)).

Figures 2.8 and 2.9 show time series of the surface radial velocity along the same radial lines as in figures 2.6 and 2.7. As the data is calculated from video filmed at an oblique angle, the velocities are inaccurate at the centre of the collapse. In this region the PIV process calculates the velocity of the falling column rather than the spreading deposit. To minimise the effect of this we chose a radius that is horizontal in the image so that we do not pick up this downwards component. The net result is that we have a region of "zero" velocity at small radii, with the radial motion hidden by the sides of the falling column.

As with the video data we can see the flow edge's initial fast acceleration, its spreading phase, and its final deceleration. The surface velocity behind the front (up to around $1\,\mathrm{m\,s^{-1}}$) is faster than the speed of the front (less than around $0.55\,\mathrm{m\,s^{-1}}$) meaning that the deposit is spreading by the front being overrun by new material

Figure 2.10 shows the deposit radius against time for a selection of the collapses. We see the initial fast acceleration, the middle slow acceleration and the final deceleration. Again we see that the collapses of the same material at different aspect ratios differ only in when they start to decelerate. Less clearly we can see that the large particles spread at a slower speed than the small ones.

Figure 2.11 shows the run-out against time for the largest aspect ratio columns $a > 5$ after the scalings

$$\hat{r} \equiv \frac{\tilde{r}}{a^{1/2}}\,, \qquad\qquad \tilde{t} \equiv \frac{t - t_f}{(h_i/g)^{1/2}}\,, \tag{2.12}$$

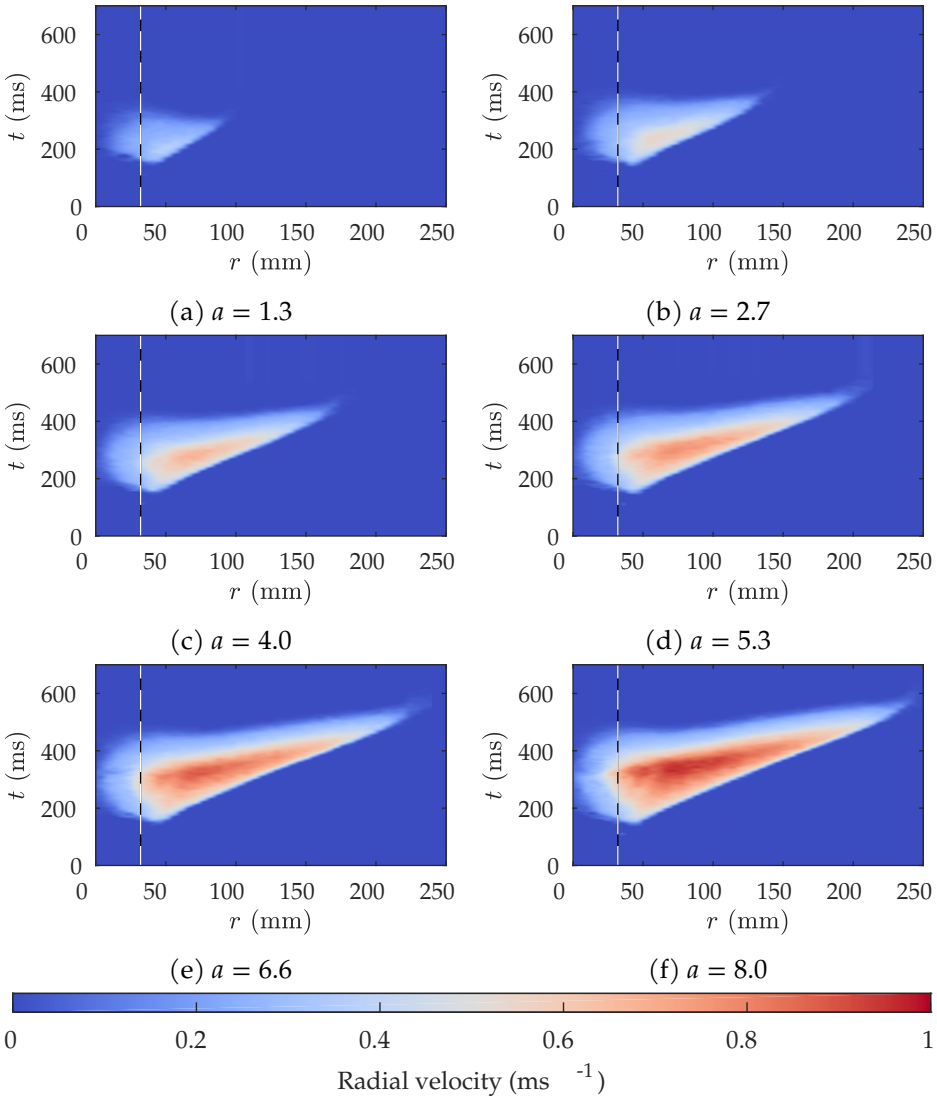

Figure 2.8: Radial velocity time series of collapses of small particles. The black and white line at 32 mm marks the initial radius of the column.

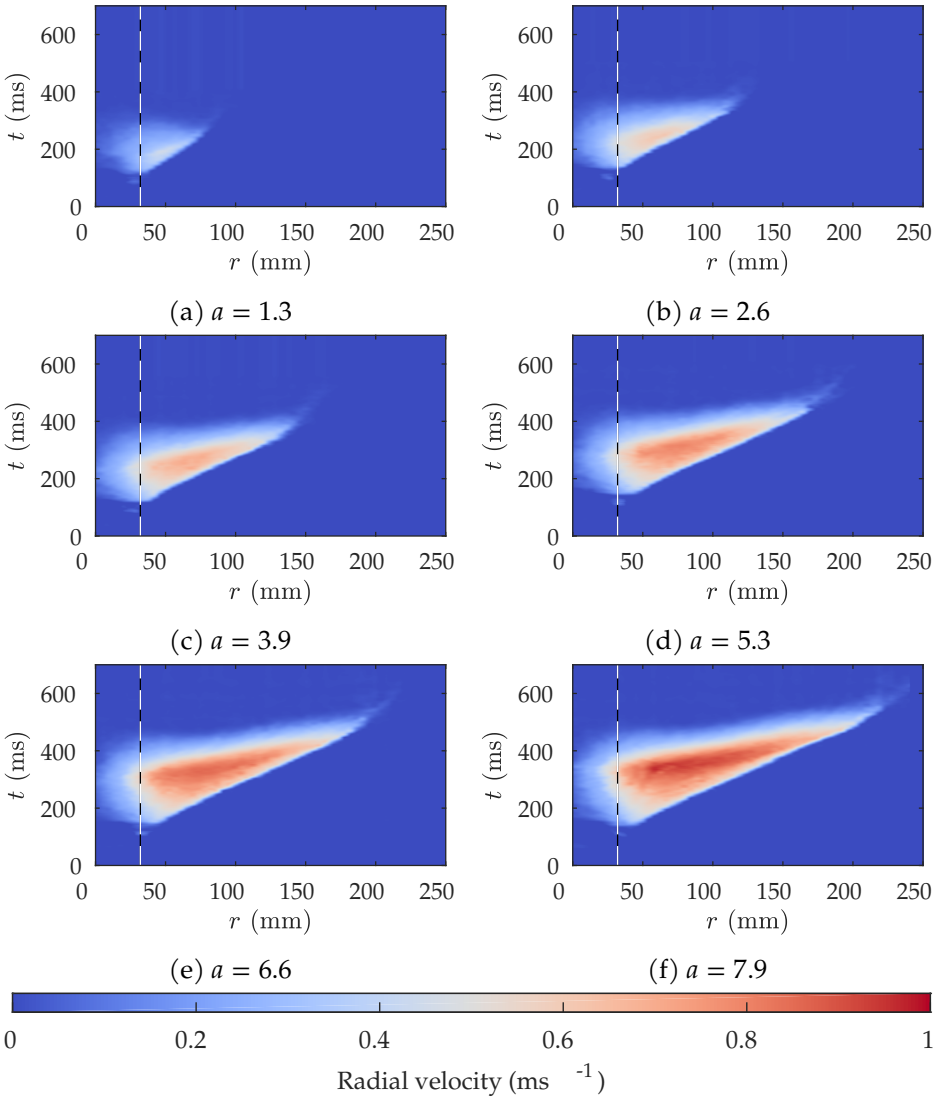

Figure 2.9: Radial velocity time series of collapses of large particles. The black and white line at 32 mm marks the initial radius of the column.

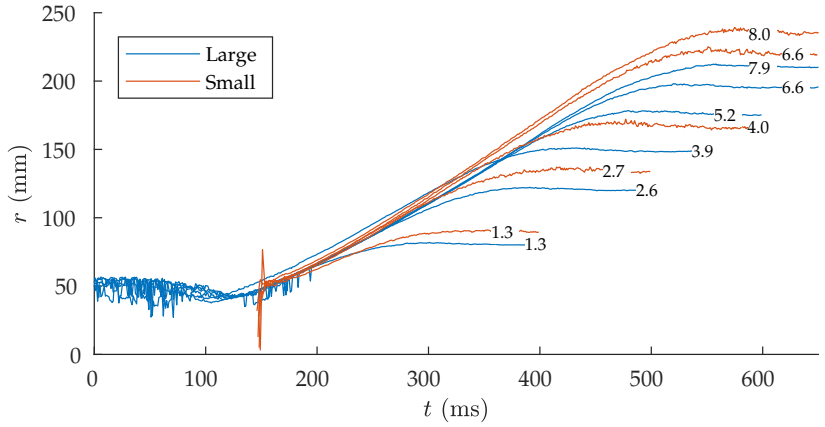

Figure 2.10: Measurements of deposit radius r against time t for a selection of collapses of each type of particle. Curves are labelled by aspect ratio.

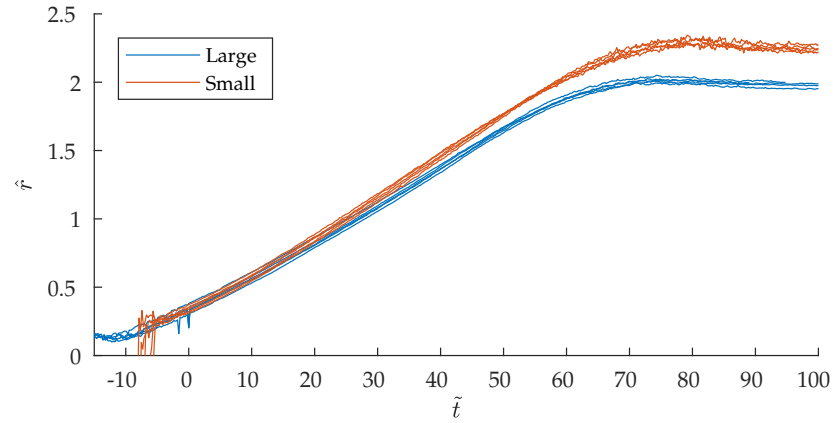

Figure 2.11: Graph showing the modified non-dimensional run-out distance $\hat{r}$ against the non-dimensional time $\tilde{t}$ for collapses with large aspect ratios ($a > 5$).

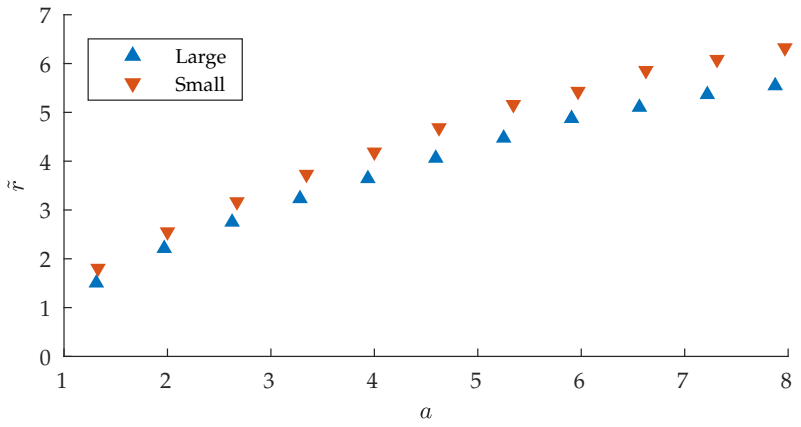

Figure 2.12: Plot of non-dimensional run-out $\tilde{r}$ against initial aspect ratio a.

where t_f is a collapse dependent value to align the curves. The run-out scaling was chosen to match that of previous work (see equations (2.3), (2.4) and (2.6)), whereas the time scaling is based on the free fall time, $(2h/g)^{1/2}$. As can be seen, all the collapses of the same material converge onto a single curve, thereby showing that these scalings are appropriate. In particular, the choice of time scaling demonstrates that the flow is controlled by the influx of new material as the column collapses. For smaller aspect ratios the fast initial acceleration and final deceleration phases dominate (as can be seen in figure 2.10) and the scalings break down.

We can also clearly see how the large particles spread at a slower speed than the small particles. Both types of collapse stop expanding at around the same non-dimensional time, causing the large particle collapses to have a small run-out distance.

Figure 2.12 shows the non-dimensional run-out for the collapses considered. Unlike in previous work, we do not see a change in behaviour between low and high aspect ratios but this is likely because we did not

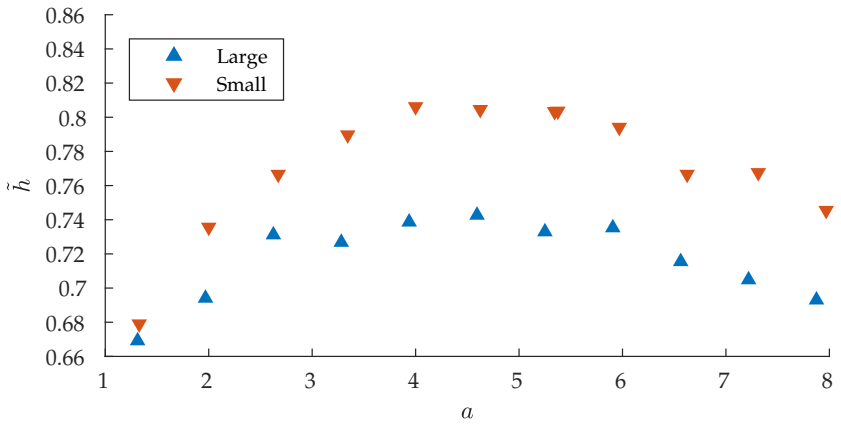

Figure 2.13: Graph of the non-dimensional final deposit height $\tilde{h}$ at $r = 0$ against the initial aspect ratio a.

perform many experiments at low aspect ratios.

More significantly, however, we observe a difference in run-out for the two materials, with the larger particles having a run-out of roughly 87% of that of the smaller ones, which corresponds to an absolute difference of 1 cm to 2 cm.

Similarly, figure 2.13 shows the non-dimensional final central height for the collapses. We see the deposit height increase with aspect ratio up to a maximum at $a \approx 4.5$. Again we see a difference between the two materials with the larger particles giving deposits with a central height of around 92% of the deposits from the smaller particles.

Although we do not have data in the low aspect ratio regime, the data we have suggests that the differences between two materials reduces as the aspect ratio tends to zero. This is consistent with previous work (e.g. Lube *et al.*, 2004) that argued that, at the lowest aspect ratios, the final deposit shape can be explained using purely geometric effects.

The combination of these two effects can be seen in their height profiles,

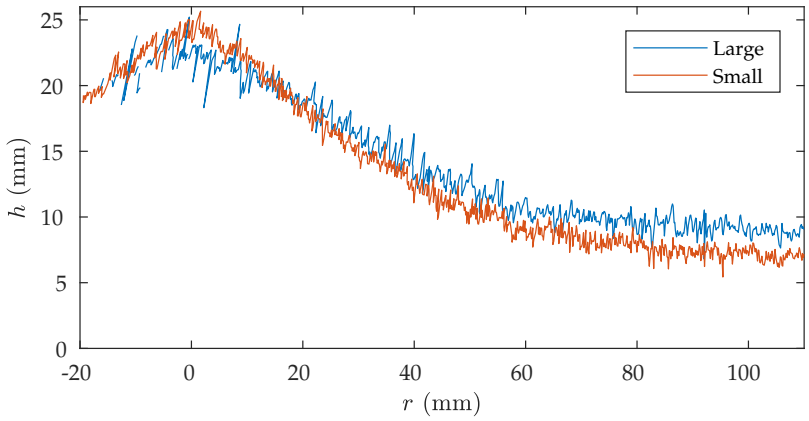

Figure 2.14: Comparison of the deposit height profiles for collapses of 1200 g of the two particle sizes. The initial aspect ratios were $a = 7.9$ (large) and $a = 8.0$ (small). Deposits extend beyond the region shown.

examples of which are shown in figure 2.14. Although the large particles have a smaller central height, their deposit has a shallower slope and so becomes thicker around 15 mm from the centre.

We can also define the *shape factor* by the ratio of the final deposit volume and the volume of a cylinder with the same maximum height and radius, i.e

$$\gamma \equiv \frac{V_f}{\pi h_{max} r_\infty^2}, \tag{2.13}$$

where V_f is the final deposit volume and h_{max} is the maximum deposit height. This quantity isolates the effect of shape of the deposit from its physical dimensions and would be 1 for a circular cylinder and 1/3 for a conical deposit. More generally, a low γ represents a deposit with a localised peak and a higher γ corresponds to a deposit that is thick for more of its extent.

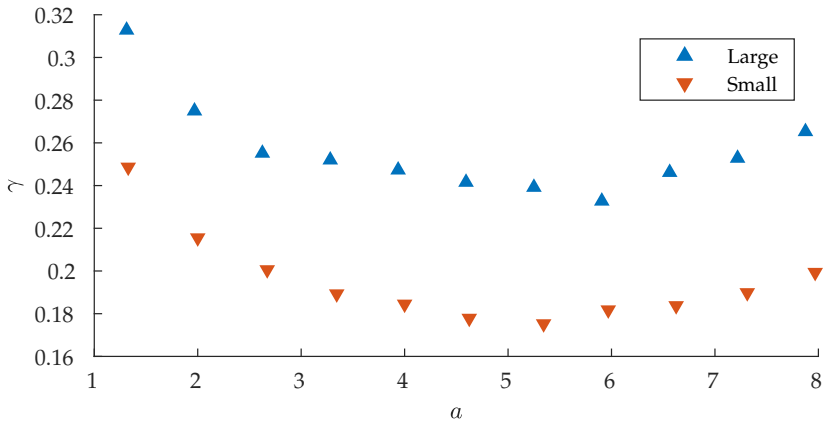

Figure 2.15: Graph of the shape factor γ against initial aspect ratio.

For our deposits the maximum height occurs at the centre of the deposit and so $h_{max} = h_i$. If we then make the additional assumption that the final deposit has roughly the same volume as the initial column (or equivalently that the initial and final packing fractions are the same) then we can get the expression

$$\gamma \approx \frac{h_i r_i^2}{h_\infty r_\infty^2}, \tag{2.14}$$

which is plotted in figure 2.15.

Both materials follow the same general trend with γ initially decreasing before reaching its minimum value at $a \approx 5$. This is consistent with previous work that found that the deposits were conical (i.e. $\gamma = 1/3$) when the aspect ratio was close to its critical value. Beyond that point the formation of a thin region around a central cone causes the value of γ to fall and give the trend we see. As we did not do any experiments in the low aspect ratio regime we do not, however, actually see the point where γ reaches $1/3$.

Beyond $a \approx 5$, γ begins to increase again. This minimum in γ corres-

ponds with the maximum in $\tilde{h}$ seen in figure 2.13, but the increase in γ shows that the rest of the deposit is not shrinking in height. The presences of bulges in the outer regions of the deposit like those observed by Lube *et al.* (2004) and Roche *et al.* (2011) would also have the effect of increasing γ.

We also see that the large particles have a γ that is approximately 30% greater than that of the small particles. This demonstrates how the large particles deposits have thicker edges than those from the smaller particles, as previously seen in figure 2.14. This difference is reasonably constant in the range of aspect ratios we considered but may differ outside of that.

2.4 Vertically split columns

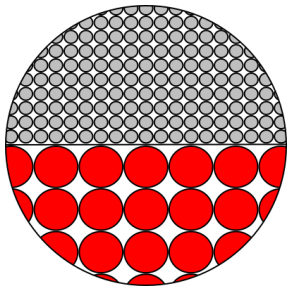

Figure 2.16: Illustration of the initial set-up for a vertically split column collapse.

In order to further investigate the differences in behaviour of the two monodisperse collapses, we considered a vertically split column as shown in figure 2.16. We inserted a cardboard sheet into the centre of a cylinder and fill each side with one of the two types of material. The cardboard can then me removed to leave a column where each half is a different material. Due to the difficulties of getting exactly the right amounts of the two materials, the top of the column is typically covered by an excess of one

material (the large particles in the case below) but this does not appear to affect the behaviour of the collapse. The cylinder had to be lifted manually due to an unsuccessful attempt to collect additional measurements.

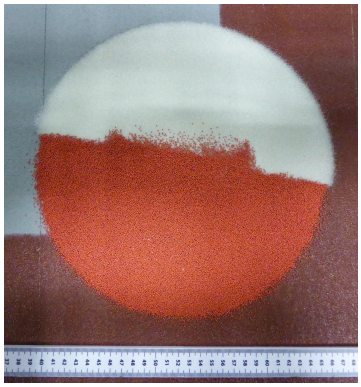

(a) Full deposit.

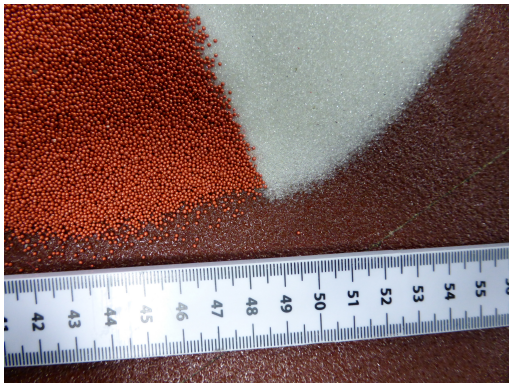

(b) Close up of the deposit edge at the interface on the right-hand side of figure 2.17a.

Figure 2.17: Photographs of the final deposit from a vertically split column collapse.

Figure 2.17 shows the results of such a collapse. As figure 2.17a shows, there is very little mixing between the two sides of the column, with any variations due to imprecisions in the set-up of the original column. As a result, we can consider the collapse as two, independent, semi-cylindrical collapses placed side-by-side, excluding a thin interfacial region.

The differences between the two half collapses can be more easily seen in figure 2.17b. The larger red beads clearly stop before the smaller white beads and the deposit is approximately 5 mm smaller in radius. This is smaller than in our earlier experiments (section 2.3), which may be due to the differences in cylinder lifting method. Both sides of the deposits are, however, surrounded by a diffuse region of particles. This extends to a similar distance for both particle types, although the individual large

particles are much more visible than the small. These are not counted in our definition of run-out (as described in section 2.2) and so are not included in the measured radii.

2.5 Discussion

Our key finding is that there are differences in the final deposits between the two sizes of particle considered. This contradicts the assertion of Lube *et al.* (2004) that the collapse process is independent of the choice of material, but it generally agrees with the findings of Lajeunesse *et al.* (2004). Like them, we found that the larger particles give deposits with a lower central height but thicker edges, but, instead of finding no differences in run-out, we found that the larger particles result in a shorter run-out distances.

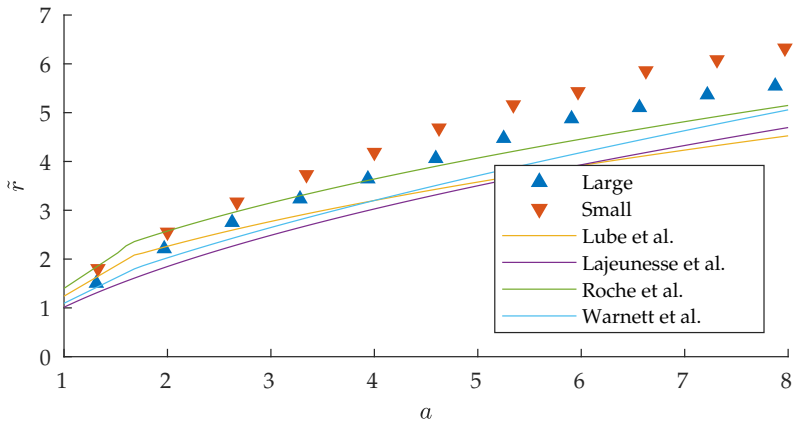

Figure 2.18: Graph of non-dimensional run-out against initial aspect ratio, compared with previously proposed laws.

Regardless of the material used, we find significant quantitative differences with previous work. Figures 2.18 and 2.19 show the previously pro-

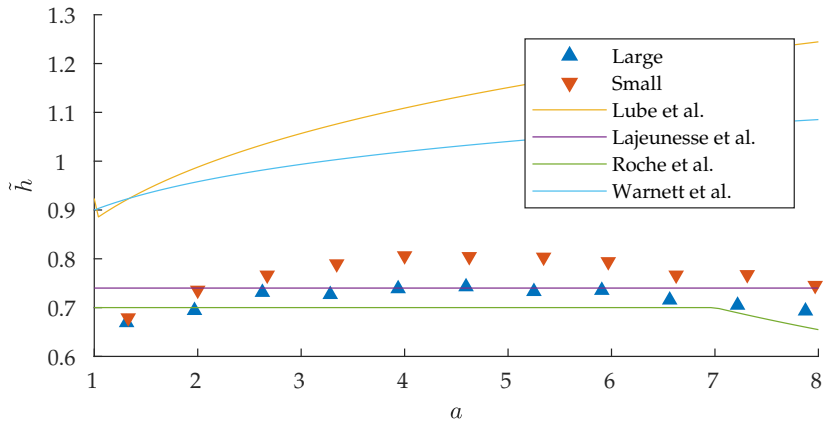

Figure 2.19: Graph of the non-dimensional central height against the initial aspect ratio, compared with previously proposed laws.

posed laws of Lajeunesse *et al.* (2004), Lube *et al.* (2004), Roche *et al.* (2011), and Warnett *et al.* (2013) compared with our data.

Compared with our experiments, the models of both Lube *et al.* (2004) and Warnett *et al.* (2013) underestimate the run-out distance but overestimate the deposit height. This can be explained by noting that both papers used materials with higher angles of repose than the glass beads used here. Even though the final deposits are far below the angles of repose, the higher friction means that the material stops sooner and can leave a taller deposit. Whilst Lube *et al.* (2004) claim that their results are independent of the choice of material, both they and Warnett *et al.* (2013) used particles with a relatively narrow range of angles of repose (30° to 35°), all of which are far higher than that of the glass beads here ($\approx 23°$).

The differences in particles would also affect the friction between them and the cylinder and the base these do not appear to be responsible for the differences in results. Whilst Warnett *et al.* (2013) do not state the material used for their cylinder, Lube *et al.* (2004) used an acrylic cylinder like we

did. Lube *et al.* (2004) found no changes in results between different base, including a smooth wooden base (like that used by Warnett *et al.* (2013)) and a sandpaper base (like that used by us).

In contrast, the laws proposed by Lajeunesse *et al.* (2004) underestimate the run-out distance but are close to the measured deposit heights. As their experiments used glass beads similar to the small particles used here, we must look for a different cause of the discrepancy. In deriving their semi-empirical law, Lajeunesse *et al.* (2004) assume that the final deposit is conical, whereas their experiments, like the deposits presented here, have a steep central cone surrounded by a region of a much shallower slope. This can also be seen in figure 2.15 which shows that the deposits have shape factors far below the value of 1/3 implicitly assumed in their analysis. The net result, and as seen in figure 2.18, is that the laws underestimate the run-out distances.

In addition, Lajeunesse *et al.* (2004) measured the run-out distances in their experiments by using a side view of their experiment but, as described in section 2.2, this method leads to undermeasurements of the run-out. As a result they find a misleading agreement between their data and their semi-empirical law. This measurement issue is likely why they found that the choice of material did not affect the run-out, despite changing the deposit shape.

The laws of Roche *et al.* (2011) come closest to matching our observations. As with Lajeunesse *et al.* (2004) they used glass beads comparable to our small particles. Although their claimed scaling for the run-out is lower than our observations at larger aspect ratios, their raw data appears to be closer to our measurements and so the discrepancy may be due to their choice of fitting.

Our observation of a decrease in the central deposit height once the aspect ratio is large enough also disagrees with the power laws proposed by Lube *et al.* (2004), Lajeunesse *et al.* (2004) and Warnett *et al.* (2013). The

law proposed by Roche *et al.* (2011) does feature a decrease for $a > 7$ but we do not have enough data at those aspect ratios to verify it. Their raw data, however, does suggest that the decrease starts at $a \approx 4$ but they do not have enough data in that region to be precise. Lube *et al.* (2004) note a decrease for $a > 10$, a more careful inspection of their data shows that the maximum actually occurs at $a \approx 5$, a value that is comparable with our findings. The data presented by both Lajeunesse *et al.* (2004) and Warnett *et al.* (2013) also features a peak at around the same aspect ratio.

3 Bidisperse collapses

Whilst the previous chapter focused on monodisperse flows, real granular flows typically feature a wide range of particle types. This introduces the possibility of *granular segregation*, whereby different types of particle separate as the flow progresses. This can have dramatic effects on the flow structure, for example the fingering instability seen by Pouliquen & Vallance (1999).

3.1 Segregation

When a mixture of two or more different particles flows due to gravity, the different species of particles tend to separate out or segregate. This can take one of two main forms: *size segregation* where larger particles rise to the surface of a flow, and *density segregation* where denser particles sink to the bottom (Drahun & Bridgwater, 1983). For simplicity we will only consider size segregation. For the types of flow present during granular collapse we expect this to primarily be due to the process of kinetic sieving.

Kinetic sieving occurs due to shearing in the flow causing gaps to open up between particles. Other particles can then fall through these gaps, with smaller particles being more likely to do so than larger particles, as illustrated in figure 3.1. As a result small particles tend to collect at the base of the flow and large particles are necessarily found towards the surface.

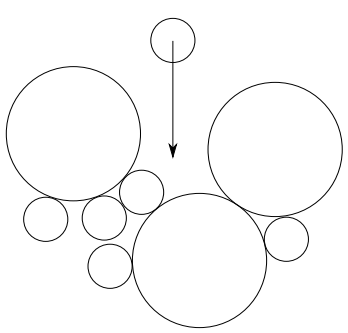

(a) A small particle can easily fall through gaps in the granular structure and accumulate near the base.

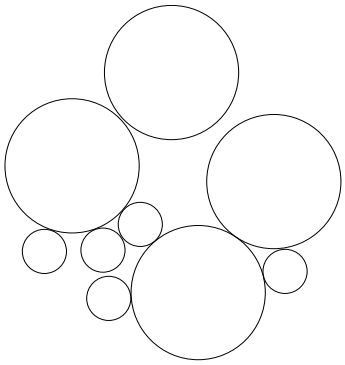

(b) Large particles cannot fall as easily and remain near the surface.

Figure 3.1: Illustration of kinetic sieving process.

3.2 Previous work

Compared to the monodisperse case there has been little research into the polydisperse granular collapse problem. Roche *et al.* (2005) performed experiments with quasi-two-dimensional collapses of bidisperse mixtures and considered the effect of fluidisation of the initial column. They only observed segregation at large particle size ratios and found that bidisperse mixtures had run-outs between those of the appropriate monodisperse collapses. The segregation mechanism varied depending on the experimental parameters, with kinetic sieving being dominant in flows with a small amount of small particles ($\lesssim 40\%$).

Phillips *et al.* (2006) also ran experiments with quasi-two-dimensional collapses of various bidisperse mixtures with very large size and shape differences between the species (e.g. 90 μm glass spheres with 75 mm × 25 mm×2.2 mm glass "rafters"). They found that the larger particles could slide over a layer of rolling particles to give a larger run-out. This set-up,

however, has little relevance to the bulk of a polydisperse flow, where the size ratio of particles is far less extreme.

Degaetano *et al.* (2013) also considered quasi-two-dimensional collapses but performed their experiments with a single-particle-wide flow. They used a fixed initial column height but varied the initial configuration and proportions of the two species of particle. They found that the flows were very similar to the monodisperse case and observed little segregation in the flows due to the segregation time scale being longer than the collapse time scale. They did, however, find that the run-out did not depend on the configuration but increased as the proportion of small particles tended towards 1/2. Their experiments, however, show strong signs of crystallisation that could have affected the dynamics of the flow and any segregation within it.

Caplan *et al.* (2014) instead considered the bidisperse axisymmetric collapse problem using two layers of either small, spherical glass beads (diameters between 300 μm and 400 μm) or large barley grains (6 mm×3 mm× 2 mm). Like Degaetano *et al.* (2013), they also found that there was little segregation in the collapses, except at the edge of the deposit where the flow is thinnest and hence less time is needed for segregation to occur. Whilst collapses with the large grains initially on top were qualitatively similar to monodisperse collapses, collapses with the small grains on top often formed a so-called detached ring of large particles. In addition, they also found that these collapses became asymmetric for larger aspect ratios due to the differences in frictional properties. Unlike Degaetano *et al.* (2013), they found that the run-out depends on the initial particle configuration, but that this could be explained by the differences in the initial potential energy of the columns due to the difference in densities of the two species. Like Degaetano *et al.* (2013), they found that the run-out distance varied with the proportions of the two species but in a more complex way.

The particles used by Caplan *et al.* (2014) meant that they could not

distinguish between the effects of differences in size, density and shape. As a result, we only used glass beads in the experiments below to isolate the effects of size differences and any segregation this might cause.

3.3 Experiments

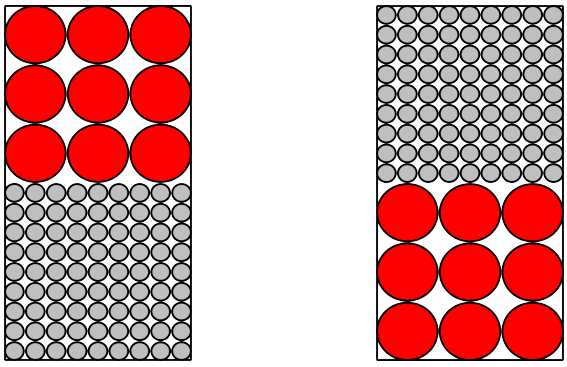

(a) Stable (b) Unstable

Figure 3.2: Illustrations of the different initial column configurations considered in these experiments.

In order to study the bidisperse problem we use the same set-up and particles as described in section 2.2 but with bidisperse initial conditions. This particular combination of particles readily segregates when flowing down a slope. Two configurations were considered, as illustrated in figure 3.2: columns with a layer of large beads above an equal mass layer of small beads (*stable*); and the inverse, with the small beads on the top (*unstable*). The terms *stable* and *unstable* refer to the stability of the configuration with respect to segregation effects. For each column configuration, the total mass of material was varied from 200 g to 1200 g, giving initial heights between 40 mm and 253 mm, and initial aspect ratios between 1.3

and 7.9.

3.4 Results

3.4.1 Flow dynamics

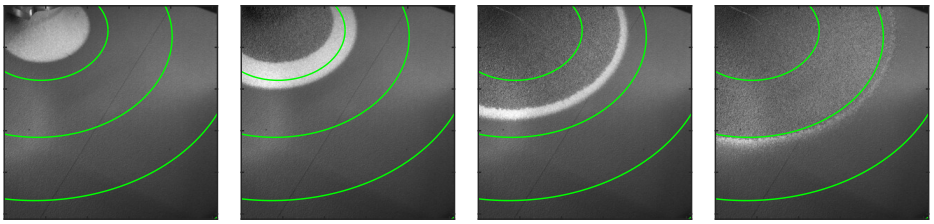

(a) Stable ($a = 7.9$)

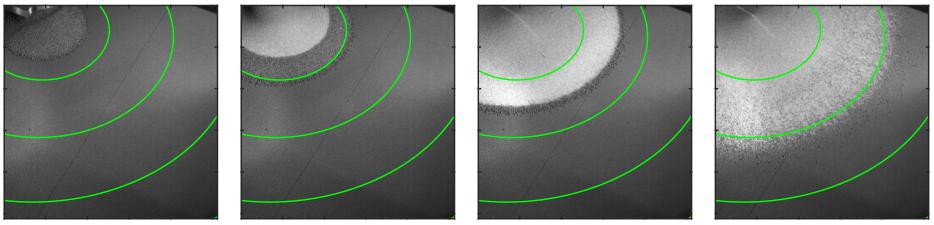

(b) Unstable ($a = 7.9$)

Figure 3.3: Images of column collapses of different types. Images are taken 200 ms, 300 ms, 400 ms and 600 ms after the start of the collapse. Green arcs are at 100 mm intervals.

The dynamics of both column types were very similar to each other over the range of aspect ratios considered as shown in figure 3.4. As in the monodisperse case, the column initially spreads axisymmetrically outwards from the base. Even once the cylinder has been retracted (figures 3.4d and 3.4e) the collapse only spreads where it hits the base and not in the falling column. The upper sections of the columns then spread over the already deposited lower sections, but we see no signs of segregation at

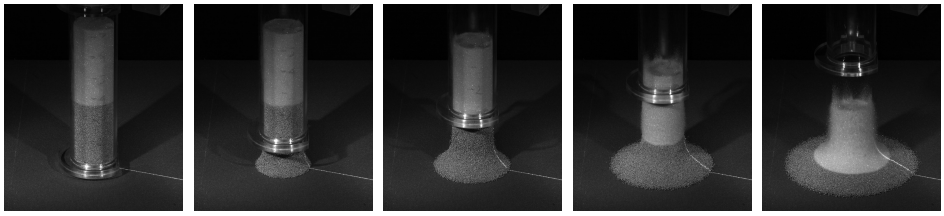

(a) 0 ms (b) 100 ms (c) 150 ms (d) 200 ms (e) 250 ms

Figure 3.4: Side view of the start of the collapse of an unstably stratified column collapse ($a = 7.8$).

this stage. Only during the final deceleration do we see some segregation in the unstably stratified columns, with the larger particles rising to the surface at the edge of the collapse, as can be seen in the last image of figure 3.3b.

Figure 3.5 shows the PIV calculated radial velocities for the same collapses at the same times as in figure 3.3. Both collapses have similar velocities to each other and to the monodisperse results (figure 2.5), although the stably stratified collapse appears to be falling faster in the centre. In neither case do we see any change in velocity associated with the interface (the black line) between the two types of particle.

Figures 3.6 and 3.7 show the time series of the raw video data. As with the monodisperse results (figures 2.6 and 2.7), we see three phases of motion: an initial fast acceleration, a sustained period of slower acceleration, and a final deceleration. We again see that the smallest aspect ratio collapses first stop at the deposit edge whereas the taller collapses first stop at the centre of the collapse. We also see particles leaving the deposit edge as the collapse stops.

The distinguishing feature of these collapses is that we can see the progress of the interface between the two materials, with the upper material appearing at later times and at the top of the images. In both cases the

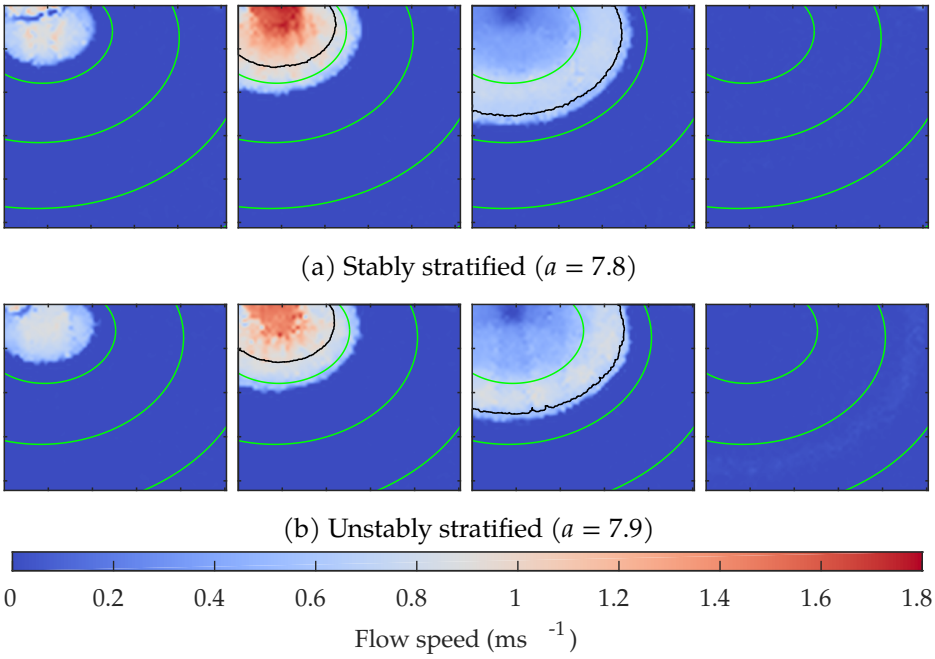

Figure 3.5: Flow speeds for column collapses of different types. Images are taken 200 ms, 300 ms, 400 ms and 600 ms after the start of the collapse. Collapses are the same as in figure 3.3. Black line show location of interface between materials where this can be clearly determined. Green arcs are at 100 mm intervals.

upper layer spreads over the lower, with the interface moving faster than the deposit edge.

Figures 3.8 and 3.9 shows the time series of the velocities for the same collapses as in figures 3.6 and 3.7 respectively. As with the velocity snapshots in figure 3.5, there is little difference between the two types of column beyond the stable columns appearing to be slightly faster. Otherwise, the data is very similar to the monodisperse collapses shown in figures 2.6 and 2.7.

Figure 3.10 shows the deposit radius against time for a subset of the

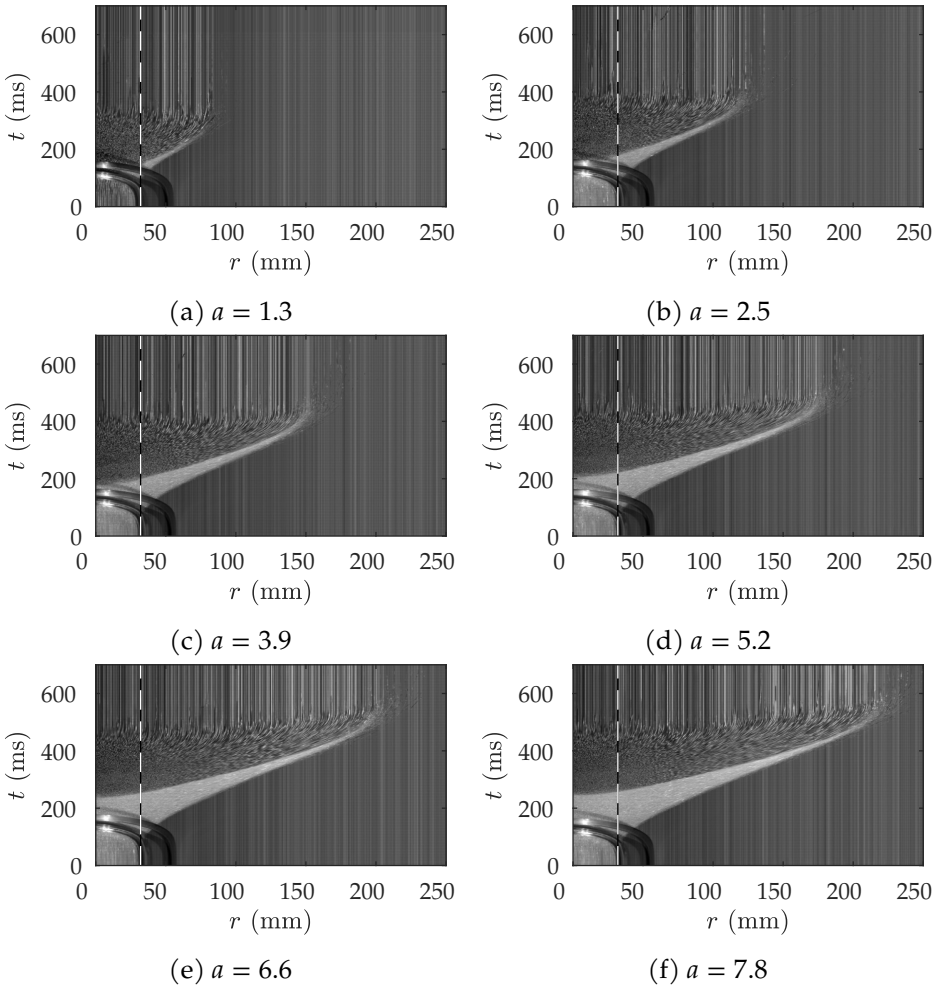

(a) $a = 1.3$ (b) $a = 2.5$

(c) $a = 3.9$ (d) $a = 5.2$

(e) $a = 6.6$ (f) $a = 7.8$

Figure 3.6: Video time series of collapses of stably stratified columns. The black and white line at 32 mm marks the initial radius of the column.

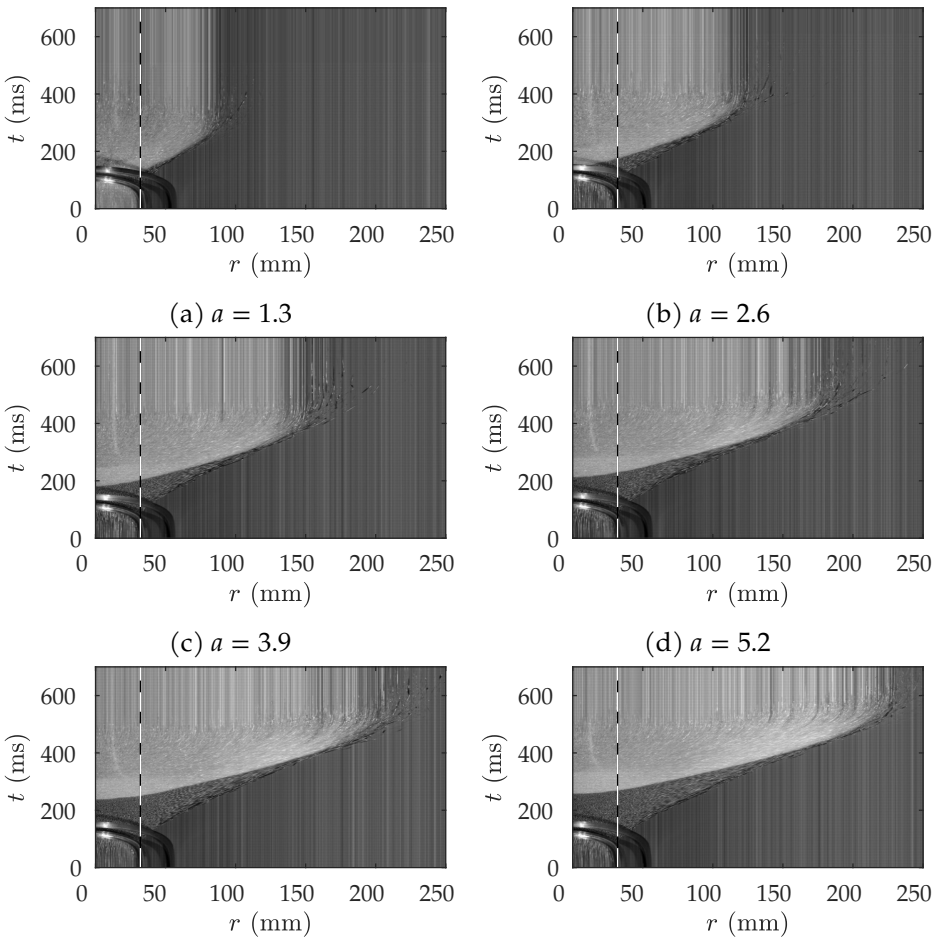

(a) $a = 1.3$ (b) $a = 2.6$

(c) $a = 3.9$ (d) $a = 5.2$

(e) $a = 6.5$ (f) $a = 7.9$

Figure 3.7: Video time series of collapses of large particles. The black and white line at 32 mm marks the initial radius of the column.

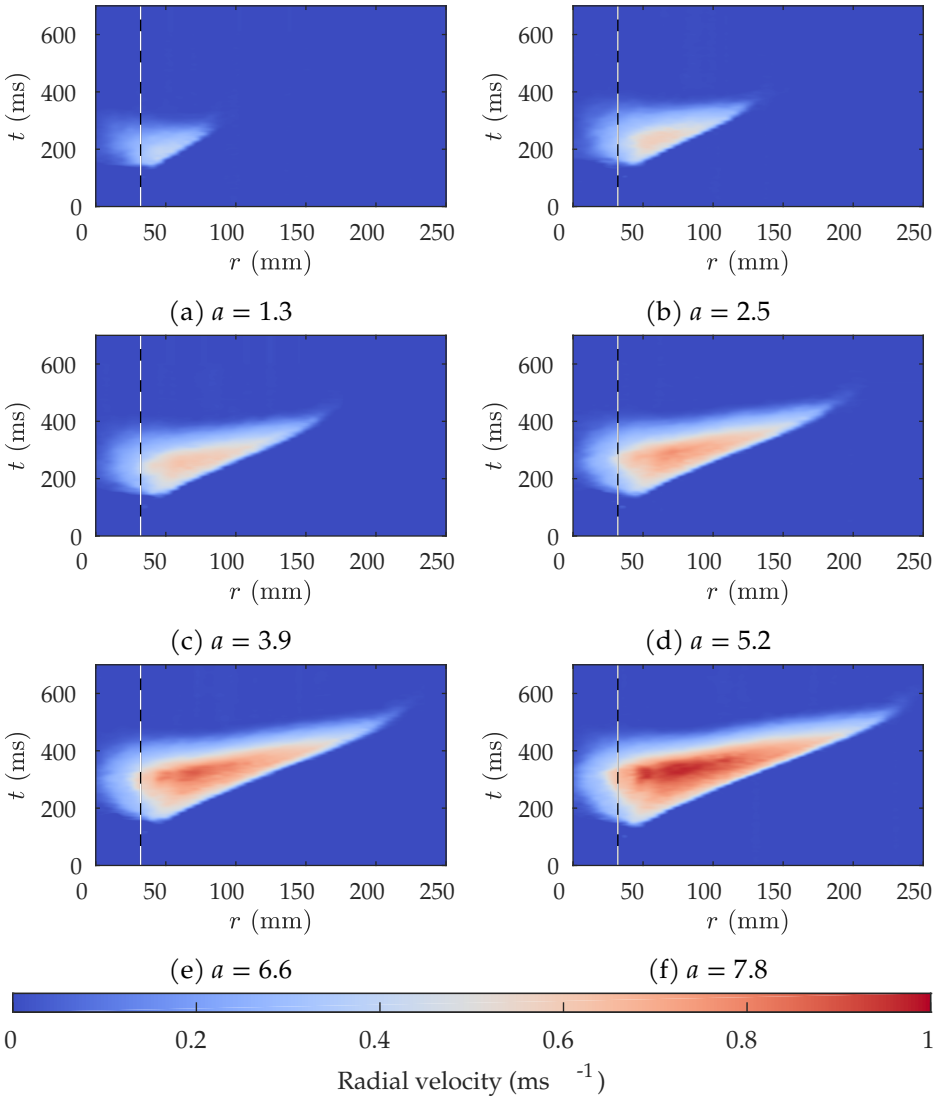

Figure 3.8: Radial velocity time series of collapses of stably stratified columns. The black and white line at 32 mm marks the initial radius of the column.

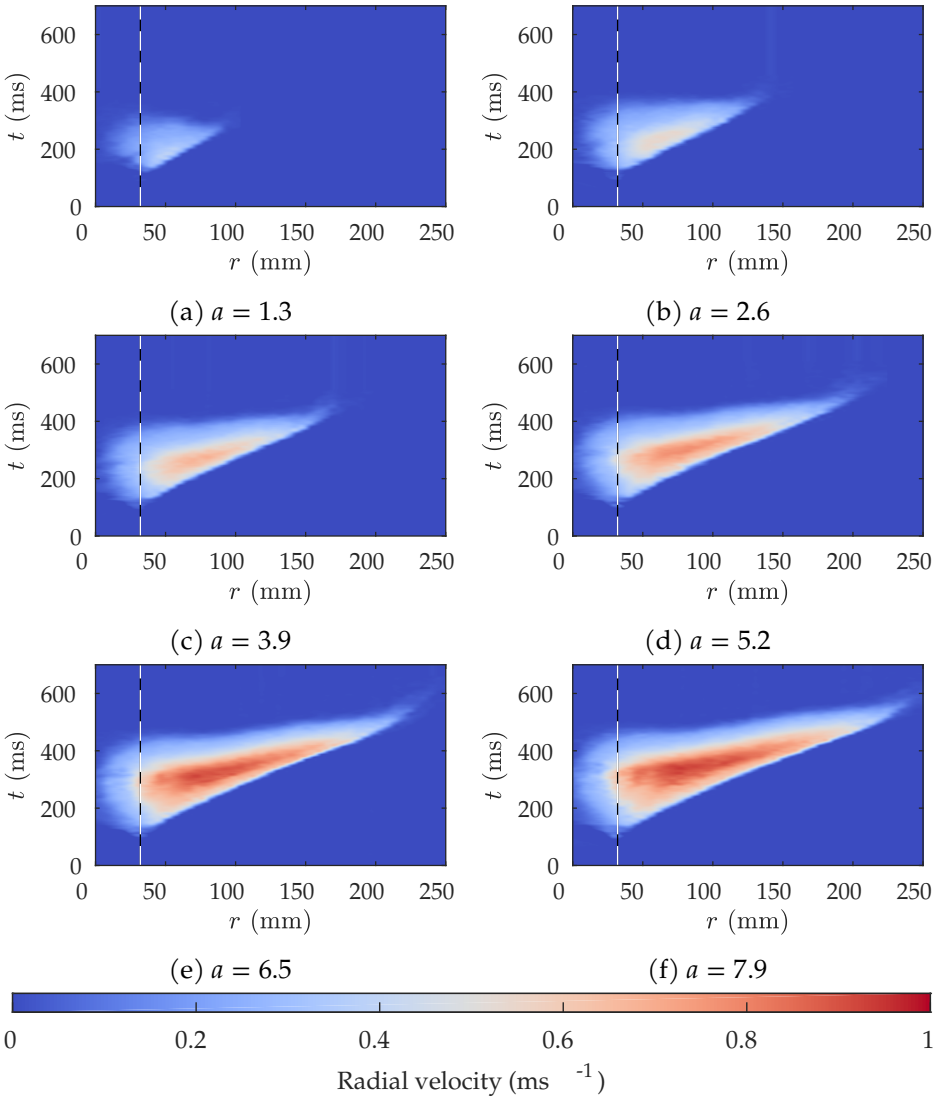

Figure 3.9: Radial velocity time series of collapses of unstably stratified columns. The black and white line at 32 mm marks the initial radius of the column.

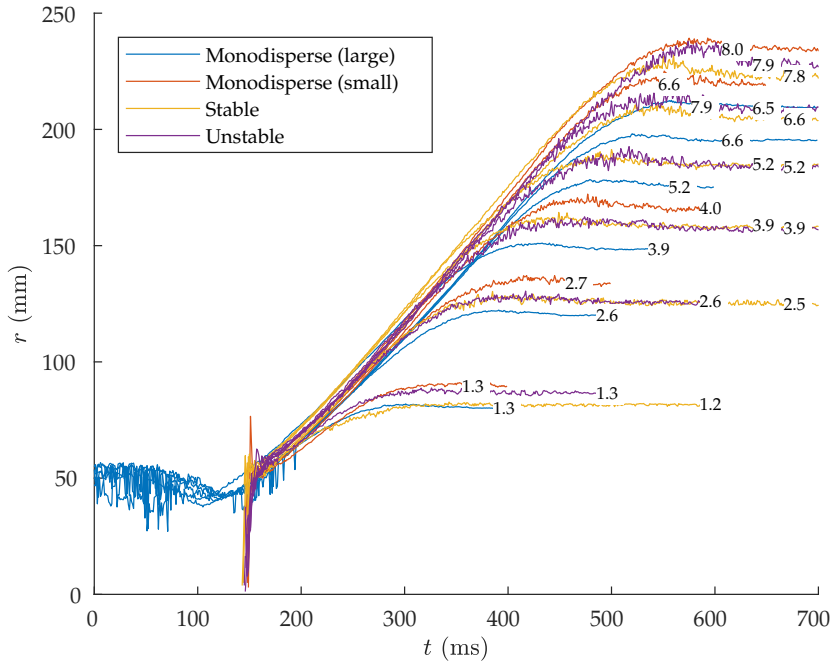

Figure 3.10: Measurements of deposit radius r against time t for a selection of collapses. Curves are labelled by aspect ratio.

mono- and bidisperse collapses considered. In this the constant spreading speed can be clearly seen, along with the shorter acceleration and deceleration phases. In particular, the spreading velocity is independent of the initial height of the column and the composition of the column. For the initial column radius used in these experiments, the spreading velocity is approximately $0.5\,\mathrm{m\,s^{-1}}$.

Figure 3.11 shows the same data but rescaled using equation (2.12) in the manner of figure 2.11. Again each type of collapse converges on a single curve with the bidisperse cases between the two monodisperse cases.

In figure 3.12 we can see the height profiles taken during the collapse of

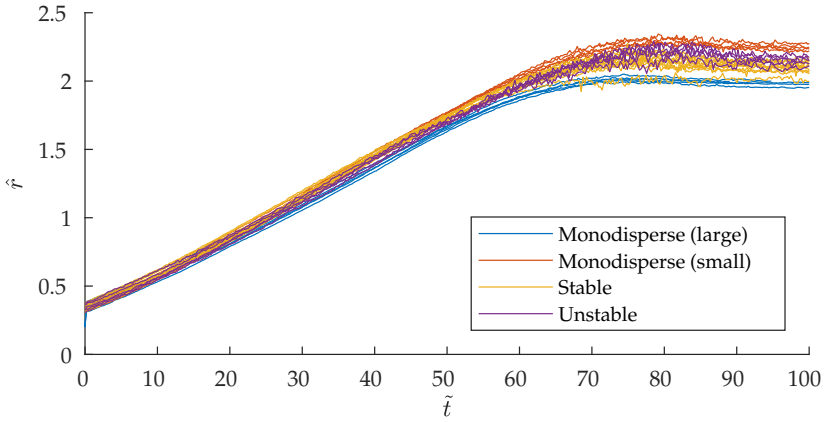

Figure 3.11: Graph showing the modified non-dimensional run-out distance $\hat{r}$ against the non-dimensional time $\tilde{t}$ for collapses with large aspect ratios ($a > 5$).

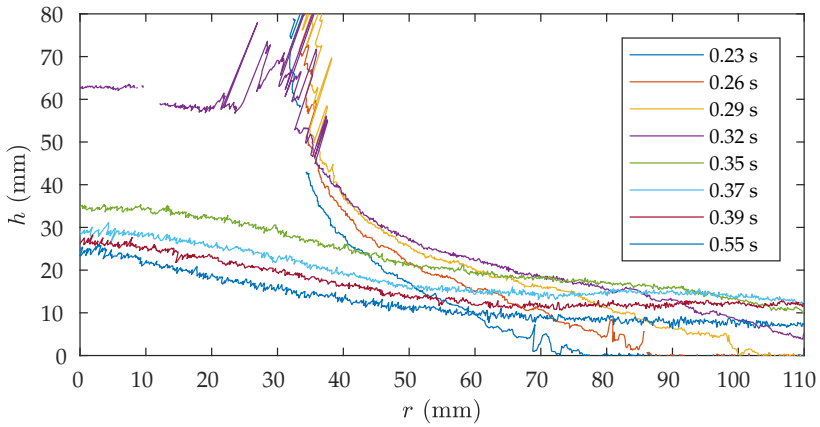

Figure 3.12: Deposit height profiles taken at various times during the collapse of a stably stratified column of aspect ratio $a = 7.2$ as measured using the laser scanner.

a typical column; the behaviour is qualitatively and quantitatively similar for all types of columns at the same aspect ratio. We can see how material moves from the centre of the collapse to the deposit edge as the collapse proceeds and the deposit thins. The noisiness of the earliest height profiles near $r = r_i$ is due to material being dragged upwards by the retracting cylinder. This can be more directly seen in figure 3.4e.

3.4.2 Final deposit

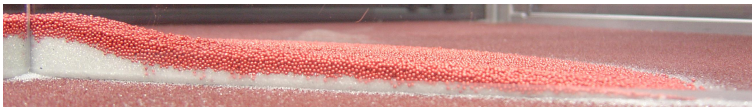

(a) Stably stratified column.

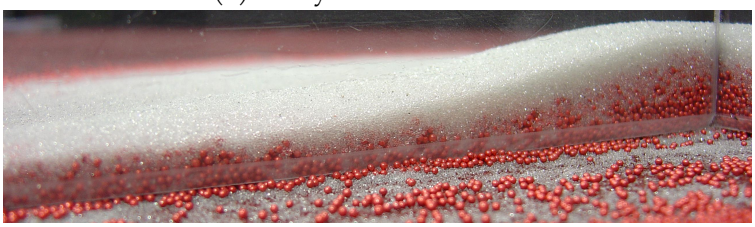

(b) Unstably stratified column.

Figure 3.13: Cross-sections of the final deposit for typical examples of the two types of column. Photographs were taken by rapidly inserting a piece of clear plastic and removing the material from one side of it.

We can observe the interiors of the deposit by inserting a transparent plastic sheet into the final deposit. Whilst this inevitably disturbs the deposit, the effect of this can be minimised with care. As expected, and as shown in figure 3.13, there is no segregation or mixing in any of the stably stratified columns, with the larger particles covering the the smaller particles. In contrast, some limited segregation can be seen in the unstably

stratified columns. This is primarily located towards the edges of the deposit where the material is thinner and there is a shear flow across the interface between the layers. Towards the centre, the smaller particles fall into the gaps between the larger ones that form as the column collapses, but is unclear whether there is any upwards motion of the larger particles. As a result, there is a mixed layer but segregation is incomplete.

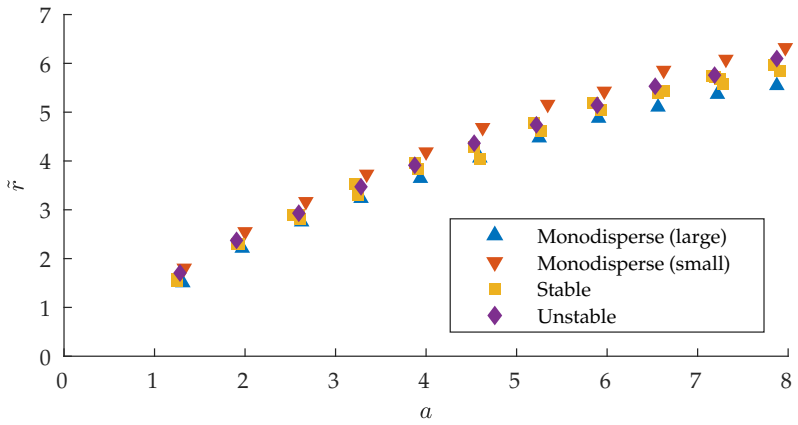

Figure 3.14: Plot of non-dimensional run-out $\tilde{r}$ against initial aspect ratio a.

Figure 3.14 shows the final non-dimensional run-out for all the collapses considered. We can see that the bidisperse collapses follow the same trends as the monodisperse collapses but with run-outs between the two types of material. In addition, the stably stratified collapses travel a slightly shorter distance than the unstably stratified ones. This is likely due to the how the measurement system defines the boundary edge, in particular the way it neglects larger particles that bounce away from the main deposit.

Figure 3.15 shows the central height of the deposit, as measured using the laser scanner, against the initial aspect ratio of the column. As with the run-outs, the heights of the bidisperse collapses lie between the mon-

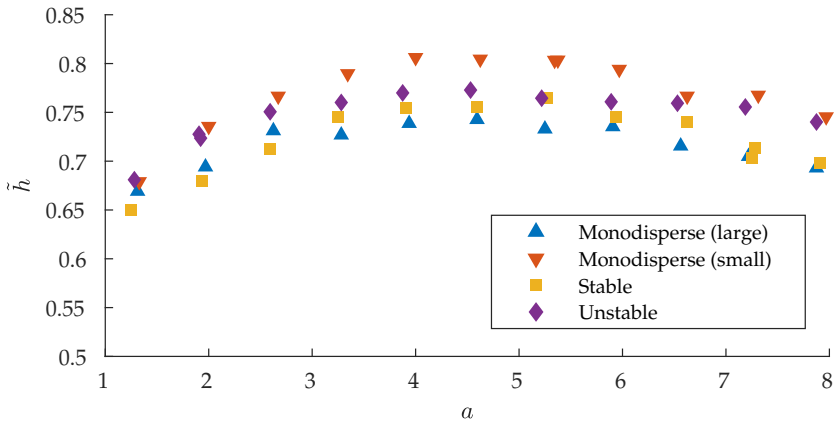

Figure 3.15: Graph of the non-dimensional final deposit height $\tilde{h}$ at $r = 0$ against the initial aspect ratio a.

odisperse ones. In addition, the deposits from stably stratified columns appear to be slightly lower at larger aspect ratios. As the aspect ratio increases, the deposit height increases until $a \approx 4.5$ whereupon the deposit height appears to decrease slightly. This is due to the top layers falling at a high enough speed that they erode the previously deposited material faster than they are themselves deposited.

Figure 3.16 shows the final height profiles of collapses of each orientation. In the region where data was collected the two profiles are almost identical except at the peak where the stably stratified collapse is slightly lower.

As with the monodisperse columns, we can calculate the shape factor as seen in figure 3.17. Again we find that the bidisperse results lie between the monodisperse ones, with the stable collapses having higher shape factors than the unstable ones.

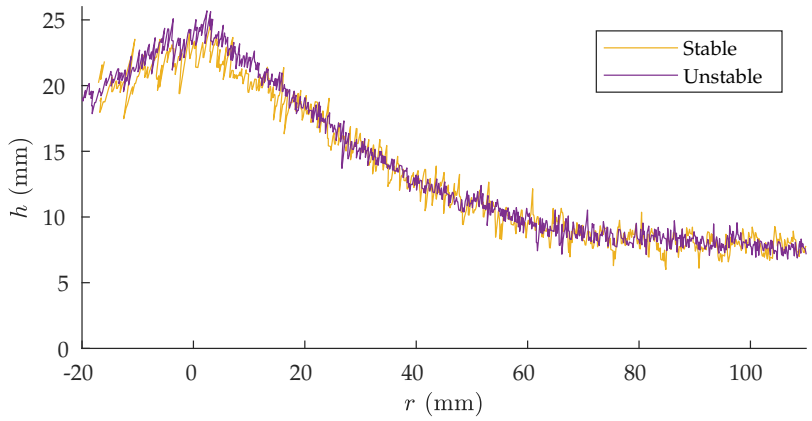

Figure 3.16: Comparison of the deposit height profiles for collapses of 1200 g of the two particle sizes. Both collapses had an initial aspect ratio of 7.9. Deposits extend beyond the region shown.

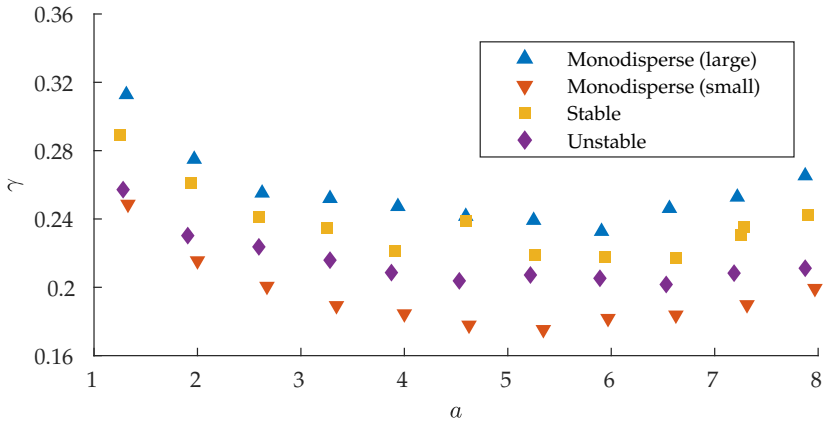

Figure 3.17: Graph of the shape factor γ against initial aspect ratio.

3.5 Different species ratios

In addition to varying the aspect ratio of the collapses, the proportions of the two media can be varied. To investigate this we considered a small

series of experiments with tube of radius 47 mm. We filled this with a total 2000 g of material in an unstably stratified initial condition, giving columns of initial heights around 192 mm and initial aspect ratios of around 4.1. We used the same materials as in the previous experiments, but varied the proportion by mass of the small beads, Π_s, between 0 and 1.

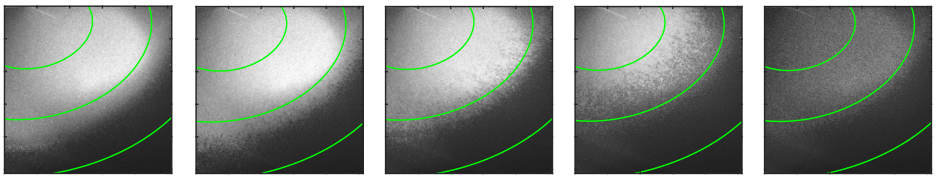

(a) $\Pi_s = 1$ (b) $\Pi_s = 0.75$ (c) $\Pi_s = 0.5$ (d) $\Pi_s = 0.25$ (e) $\Pi_s = 0$

Figure 3.18: Final deposits for unstably stratified columns of mass 2000 g, initial radius 47 mm and a range of different proportions of small particles Π_s. Green arcs are at 100 mm intervals.

Figure 3.18 shows the final deposits for the collapses considered. All the collapses are broadly similar to each other and to the collapses in figure 3.3. Whilst there is some segregation present at the interface between the two species, the initial distribution of the particles in the primary cause for their final positions. For $\Pi_s = 0.75$ the lower layer of large particles is too thin to spread the full width of the deposit and is almost completely overrun by the higher layer of small particles. For $\Pi_s = 0.25$, however, the lower layer is so thick that the small particles cannot overrun it, leaving a region of large particles at the flow edge. In the intermediate case of $\Pi_s = 0.5$ the small particles reach the deposit edge only at the very end of the flow. As a result the edge contains both types of particle.

This can be indirectly seen in figure 3.19. As discussed in section 2.4, the two monodisperse cases have significantly different run-outs. More surprisingly, the $\Pi_s = 0.25$ and $\Pi_s = 0.75$ cases are, respectively, almost identical to the $\Pi_s = 0$ and $\Pi_s = 1$ cases. This suggests that the collapse

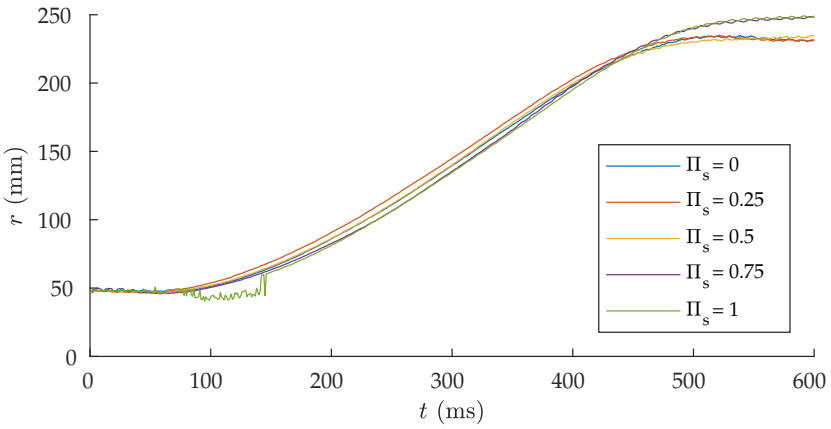

Figure 3.19: Graph of the deposit radius against time for unstably stratified columns with varying proportions of small particles.

spread is controlled by the type of particle at the edge: the material at the centre merely provides a source of energy and matter.

The $\Pi_s = 0.25$ and $\Pi_s = 0$ collapses, however, appear to have the run-out fall when $t \approx 500\,\text{ms}$. This is due to large particles bouncing away from the deposit edge, thereby reducing the radius of the central deposit and hence the measured run-out. Without this effect the collapses would have a similar run-out to the $\Pi_s = 0.5$ one.

Like the two collapses discussed above, the $\Pi_s = 0.5$ case has large particles at the edge for the majority of the collapse, giving it the same run-out distance as for the $\Pi_s = 0$ case. At the very end of the collapse, though, the small particles reach the flow front and do not escape in the same way that large particles do. As a result, we do not see the same drop in measured run-out.

3.6 Mixed columns

Whilst all of the work we have so far presented in this chapter used layered columns, we also considered the possibility of using a mixed column. The existence of segregation means that mixing granular media is a notoriously hard problem (see, e.g., Bridgwater (2012)). As a result we performed some basic experiments to see whether it was possible to obtain a well mixed initial state.

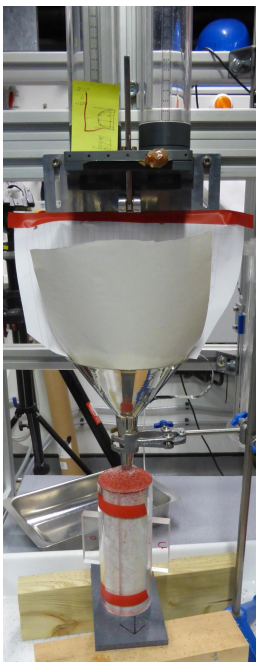

Figure 3.20: Photograph of the apparatus for filling mixed columns. The two acrylic tubes at the top of the image were each filled with one of the two species of particle. The metal lever is then pulled, retracting a metal plate, and allowing the particles to fall through the funnel and into the tube.

Figure 3.20 shows our basic set-up. The two acrylic tubes are filled with

the two species of particles. By pulling the metal lever a plate is retracted, thereby allowing the two species to flow into the funnel at an equal rate. The particles then bounce around the funnel, thereby giving an approximately mixed outflow. This then used to completely fill a vertically split acrylic cylinder. The tube is then capped, rotated so that it is horizontal, and the upper half of the cylinder is removed and excess material scraped away to give a flat surface. Whilst there is some disturbance, particularly at the original top of the column, this gives an approximate cross-section of the column.

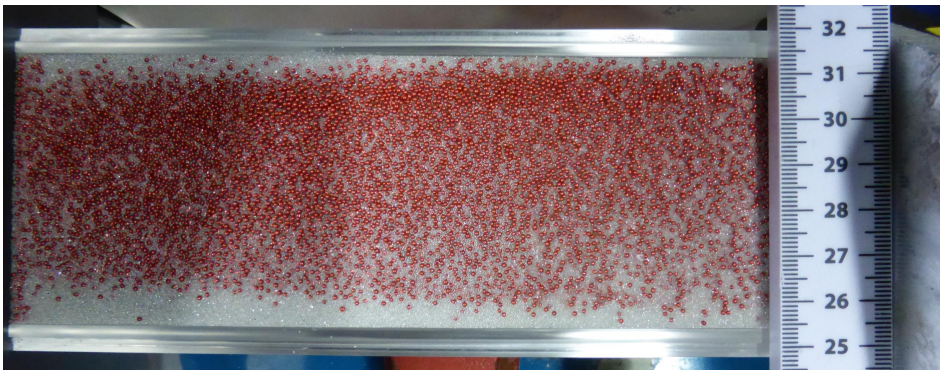

Figure 3.21: Photograph of the interior of a mixed column. The top of the column is to the right of the image.

A typical example cross-section can be seen in figure 3.21. A clear radial variation is visible, with the small particles collecting at the edges. Figure 3.20 also demonstrates this effect as very few large particles can be seen through the cylinder wall. By filming the filling process, as seen in figure 3.22, we can see that is due to the difference in behaviour between the two particle types as they hit the top of the filling cylinder. The larger particles hit the free surface and avalanche down it, whereas the small particles bounce off it allowing them to reach the edge before the large particles.

Figure 3.22: Still image from video of filling process. A cloud of bouncing small particles can be seen above an avalanching mound of large particles at the free surface. The incoming stream is not vertical, despite the funnel being so.

In addition to this there is a horizontal variation (top to bottom in image) in the particle distribution due to the difficulty of getting a vertical stream of particles. Despite the funnel spout being aligned vertically, asymmetries in the system cause the particles to flow out at an angle, as seen in figure 3.22. Combined with the radial effects described above, this leads to a separate horizontal variation in the particle distribution.

The thin layer of large particles at the bottom of the column (left of image) is due to transient behaviour at the start of the flow. As the small particles bounce higher, it means that it takes longer for the first of them

to settle and hence only large particles are present in the lowest region of the column.

As well as this, the thickness of the small particle region at the column edge shrinks towards the top of the column (right of image). As the funnel and filling apparatus was held at a fixed height, these particles fell a shorter distance than those at the bottom of the column. This means they hit the free surface at lower speeds and, hence, bouncing effects would be expected to be less significant, thereby giving less radial variation.

Finally, and as seen in figure 3.20, the very top of the column is almost purely large particles. This is because of segregation as particles flow over and settle on the top of the column.

All of the asymmetries could be due to the process of scraping the cross-section flat. This, however, would be expected to spread the large particles across the surface. As the key asymmetry is due to a lack of large particles in a region, this is unlikely to be an artifact of the scraping.

Whilst different filling procedures would change the importance of the effects mentioned above, there is no way to eliminate them all. The alternative approach of mixing the materials in situ is impractical considering the narrowness of the cylinder (radius of 32 mm) and the high aspect ratios used (up to 8).

The combination of all these asymmetries means that we did not pursue the idea of mixed columns further. As there is no feasible and non-destructive way of viewing the interior, we cannot know the initial state of the column. This means we cannot distinguish variations in the final distribution of the two types due to the collapse dynamics from those caused by variations in the initial distribution. As our mixed columns showed vertical variations in particle distribution, it means that this method cannot be used if we want to vary the initial height as we could not get the same distribution for each different height.

3.7 Discussion

Our key finding is that segregation is not a significant factor in the large scale dynamics of bidisperse column collapses. Whilst the particles we used readily segregate in other flows, e.g. chutes flows and the filling flows in section 3.6, they do not in column collapses, contrary to our initial expectations. Both types of bidisperse column behaved almost identically to the monodisperse collapses that have been previously studied, with similar power laws for the run-out distance to earlier work. Whilst some segregation is observed in the unstably stratified columns, it is incomplete and does not appear to have any effect of the bulk flow. This lack of segregation is primarily due to the lack of time in which it can occur, with each collapse lasting less than 1 s from start to finish. In addition, there is no significant shear across the interface between the two types of particles for much of the flow. This further reduces the amount of time available for particles to segregate. As a result, segregation can only take place towards the end of the collapse, when the deposit is at its thinnest.

We must also reconcile our findings with the results of Caplan *et al.* (2014), where significant differences were found between the bi- and monodisperse collapses. In that work a smooth base surface was used, which led to particles sliding at the edge of the deposit. This was hypothesised to be the cause of the detached rings that were observed. In the present work, we used a rough base in order to prevent particles from sliding or rolling. As expected, this eliminated the differences in deposit shape. As both of our particle types were the same shape, we also removed the possibility of a fingering-like instability (as in, e.g. Pouliquen *et al.*, 1997), meaning that we did not observe any asymmetric deposits.

4 Very high aspect ratio collapses

4.1 Motivation

As discussed in section 2.1, previous work has found a variety of different laws for the run-out distance and for the deposit height. Whilst these laws are similar for small aspect ratio collapses, they diverge significantly for very large aspect ratios. Of the papers discussed, only Roche *et al.* (2011) really consider aspect ratios much large than 10. They observe significant changes in the flow dynamics with the appearance of a series of radially expanding circular waves at large aspect ratios. The final deposits also changes, with a large circular ridge around a central cone. As this regime was not the primary focus of their paper they do not go in to much detail and so deserves further study.

Although there has been some numerical work at even higher aspect ratios (Lagrée *et al.*, 2011; Riber, 2017), this has predominately been in two dimensions and lacks experimental validation.

In this chapter we use general scaling arguments to restrict the range of laws that could possibly be valid in the limit of $a \to \infty$. We then describe some initial experimental work into very high aspect ratio collapses.

4.2 Large aspect ratio asymptotics

In order to understand the collapse behaviour at very high aspect ratios, we can consider the geometry of the final deposit as the aspect ratio $a \to \infty$.

To do this we will use big-O notation and write

$$f = O(g) \Leftrightarrow |f(a)| \leq M\,|g(a)|\ \forall a \geq A, \tag{4.1}$$

for some functions $f(a)$ and $g(a)$, and constants $M > 0$ and A. We will also use the inverse

$$f = \Omega(g) \Leftrightarrow g = O(f). \tag{4.2}$$

In particular, $f = O(1)$ means that, for large enough a, $f(a) \leq M$ for some constant $M > 0$. As we will only consider positive quantities, we also note that $f = \Omega(1)$ means that $f(a) \geq N$ for some constant $N > 0$, again for large enough a.

For simplicity we will assume that the deposit is axisymmetric, but the following analysis could be extended to certain classes of asymmetric deposits. We will also take the limit $a \to \infty$ with a fixed initial radius r_i. Our problem can then be written in terms of: the aspect ratio a, the maximum height of the final deposit $h_{max}(a)$, the final deposit radius $r_\infty(a)$, and the shape factor

$$\gamma(a) \equiv \frac{V_f}{\pi h_{max} r_\infty^2}, \tag{4.3}$$

as in equation (2.13), where $V_f(a)$ is the final deposit volume. For notational clarity we will not explicitly write the dependency on a.

We will also assume that the packing fraction of the final deposit is independent of the size of the initial column for large enough aspect ratios or, equivalently, that the volume of the final deposit is a constant multiple of the volume of the initial column. Hence we have

$$V_i = \pi h_i r_i^2 = k\pi\gamma h_{max} r_\infty^2 = kV_f. \tag{4.4}$$

Note that we must have $0 \leq \gamma \leq 1$ and hence that

$$\gamma = O(1). \tag{4.5}$$

If we assume that the deposit always remains connected then we must have a minimum deposit depth h_{min} at all points given by the average height of a single grain of the material. As this is a property of the material it is constant as $a \to \infty$ and hence

$$h_{max} = \Omega(1). \tag{4.6}$$

We now assume that our granular material has a constant angle of repose $\theta_r < 90°$ and that any slope above this angle will avalanche. If we apply this condition across the whole of the final deposit we must therefore have

$$h_{max} \leq r_\infty \tan\theta_r, \tag{4.7}$$

and hence

$$h_{max} = O(r_\infty). \tag{4.8}$$

If we now apply equation (4.7) to equation (4.4) and recall that $\gamma \leq 1$ we find that

$$k\gamma r_\infty^2 h_{max} = r_i^2 h_i \tag{4.9}$$

$$k r_\infty^3 \tan\theta_r \geq a r_i^3, \tag{4.10}$$

and hence

$$r_\infty = \Omega\left(a^{1/3}\right). \tag{4.11}$$

We now note that the existence of a minimum deposit depth, h_{min}, means that, for any given h_{max} and r_∞, there is a minimum, non-zero value of γ. Using axisymmetry and the existence of an angle of repose, this is ob-

tained by a deposit that comprises a central cone at the angle of repose θ_r surrounded by a disc of material at the minimum deposit depth h_{min}. This has a volume of

$$V_f = \pi h_{min}\left(r_\infty^2 - h_{max}^2 \cot^2\theta_r\right) + \frac{1}{3}\pi h_{max}^3 \cot^2\theta_r, \tag{4.12}$$

and hence

$$\gamma_{min} = \frac{h_{min}}{h_{max}}\left(1 - \frac{h_{max}^2}{r_\infty^2}\cot^2\theta_r\right) + \frac{h_{max}^2}{3r_\infty^2}\cot^2\theta_r. \tag{4.13}$$

Equation (4.8) means that the second term is at most the same order as the first first term, but we can say nothing about the third term. Hence we can only conclude that

$$\gamma = \Omega\left(h_{max}^{-1}\right) \tag{4.14}$$

$$= \Omega\left(h_{max}^2 r_\infty^{-2}\right), \tag{4.15}$$

or equivalently

$$\gamma h_{max} = \Omega\left(1\right), \tag{4.16}$$

$$\gamma r_\infty^2 = \Omega\left(h_{max}^2\right). \tag{4.17}$$

Applying equation (4.4) then gives us that

$$r_\infty^2 = O\left(a\right), \tag{4.18}$$

$$h_{max}^3 = O\left(a\right). \tag{4.19}$$

Collecting all of these we conclude that

$$h_{max} = \Omega(1) \tag{4.20}$$
$$= O\left(a^{1/3}\right), \tag{4.21}$$
$$r_\infty = \Omega\left(a^{1/3}\right) \tag{4.22}$$
$$= O\left(a^{1/2}\right), \tag{4.23}$$
$$\gamma = \Omega\left(h_{max}^{-1}\right) \tag{4.24}$$
$$= \Omega\left(h_{max}^2 r_\infty^{-2}\right) \tag{4.25}$$
$$= O(1), \tag{4.26}$$
$$h_{max} r_\infty^2 \gamma \sim a. \tag{4.27}$$

Although these results do not require it, we can follow previous work and suppose that h_{max}, r_∞ and γ follow power laws. If we consider $h_{max} \propto a^H$, $r_\infty \propto a^R$ and $\gamma \propto a^\Gamma$ then we obtain:

$$0 \leq H \leq \frac{1}{3}, \tag{4.28}$$
$$\frac{1}{3} \leq R \leq \frac{1}{2}, \tag{4.29}$$
$$\Gamma \geq -H, \tag{4.30}$$
$$\Gamma \geq 2(H - R), \tag{4.31}$$
$$\Gamma \leq 0, \tag{4.32}$$
$$H + 2R + \Gamma = 1. \tag{4.33}$$

4.2.1 Discussion

Before comparing these findings with previous work we must note that for large run-outs $\tilde{r} = (r_\infty - r_i)/r_i \to r_\infty/r_i$, and so the two quantities are interchangeable when discussing large aspect ratio collapses. For the collapses previously considered, the maximum height occurs at the centre

of the deposit (i.e. $\tilde{h} = h_{max}/r_i$), but this need not hold for larger aspect ratio collapses.

An immediate finding of our analysis is that Warnett *et al.* (2013) cannot be correct when they argue that $\tilde{r} \sim a^{0.66}$ for large a. We cannot, however, rule out it being appropriate for the range of aspect ratios they considered. Our argument is, however, consistent with the $\tilde{r} \sim a^{1/2}$ behaviour of Lube *et al.* (2004) and Lajeunesse *et al.* (2004). It also allows their respective claims of $\tilde{h} \sim a^{1/6}$ and $\tilde{h} \sim 1$. It is worth noting that Lajeunesse *et al.* (2004) derive their results using mass conservation (our equation (4.4)) along with their observations that h_{max} tended to a constant and the specific deposit shapes that they observed (and hence a specific, fixed γ).

The laws of Roche *et al.* (2011) are more complicated to evaluated. As they have $\tilde{h} \propto a^{-1/2}$ they fail to satisfy equation (4.20) and so are disallowed by our analysis. However, they observe that their higher aspect ratio collapses give deposits that feature a ridge around a central cone. As the aspect ratio increases they found that this ridge becomes similar in height to that of the central cone. It is thus conceivable that at even higher aspect ratios the ridge becomes taller than the central cone and so $\tilde{h} \neq h_{max}/r_i$. If this occurs then our conditions no longer apply to their laws.

An interesting, but unobserved, case is when both r_∞ and $h_{max} \sim a^{1/3}$, and γ is constant. In these cases the deposit keeps a fixed shape but expands equally in all dimensions. Whilst this has not yet been seen in any collapse experiments, we might expect the collapsing material to reach a terminal velocity once a is large enough. The problem then becomes identical to the problem of the deposit from a draining funnel which gives a cratered cone with the required behaviour for r_∞ and h_{max}.

4.2.2 Two dimensions

The above arguments can be easily adapted to two dimensions and this gives

$$h_{max} = \Omega(1) \tag{4.34}$$
$$= O\left(a^{1/2}\right), \tag{4.35}$$
$$r_\infty = \Omega\left(a^{1/2}\right) \tag{4.36}$$
$$= O(a), \tag{4.37}$$
$$\gamma = \Omega\left(h_{max}^{-1}\right) \tag{4.38}$$
$$= \Omega\left(h_{max} r_\infty^{-1}\right) \tag{4.39}$$
$$= O(1), \tag{4.40}$$
$$h_{max} r_\infty^2 \gamma \sim a. \tag{4.41}$$

And if we again assume $h_{max} = a^H$, $r_\infty = a^R$ and $\gamma = a^\Gamma$,

$$0 \leq H \leq \frac{1}{2}, \tag{4.42}$$
$$\frac{1}{2} \leq R \leq 1, \tag{4.43}$$
$$\Gamma \geq -H, \tag{4.44}$$
$$\Gamma \geq H - R, \tag{4.45}$$
$$\Gamma \leq 0, \tag{4.46}$$
$$H + R + \Gamma = 1. \tag{4.47}$$

Whilst there a large variety of different values for H and R have been found in previous work, they generally fall within these values.

4.3 Experiments

4.3.1 Experimental set-up

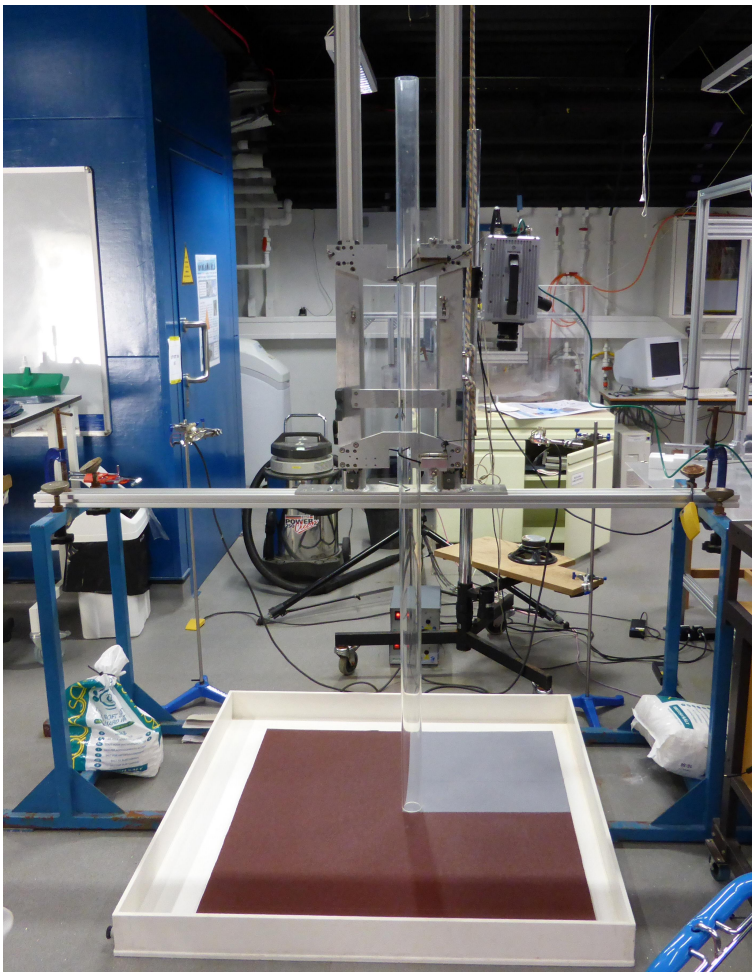

Figure 4.1: Photograph of the very tall collapse apparatus.

To increase the maximum aspect ratio we first used the apparatus pic-

tured in figure 4.1. We used an acrylic tube of height 2 m and inner radius 25 mm, with the smaller radius allowing us to achieve higher aspect ratios whilst aiming to avoid being so narrow that wall effects become significant. Due to the length of the cylinder we could not use a pneumatic system as in the previous experiments. Instead we strapped the cylinder to a carriage that could be manually raised by pulling on a rope. The cylinder was lifted as fast and as high as possible, but it could be lifted no higher than approximately 1.8 m due the experimenter's lack of height. This was, however, sufficient to ensure that the granular material left the cylinder before the cylinder reached its highest point.

4.3.2 Glass beads

We start by directly extending the experiments of section 2.2 by considering collapses of 300 μm to 425 μm glass beads. We varied the initial mass of material from 500 g to 3500 g (corresponding to aspect ratios between 6.2 and 46.3). Results for higher aspect ratios were not possible due to material running off the edge of the base.

The final deposits of these experiments can be found in figure 4.2 and figure 4.3. The smallest collapse considered with $a = 6.2$ is in the regime considered in chapter 2 and the final deposit is typical of those experiments. As the aspect ratio increases an asymmetry begins to appear at $a \approx 10$ (between figure 4.2b and figure 4.2c) and grows larger as the aspect ratio increases.

Figure 4.3 shows photographs of the final deposit with a vertically projected laser sheet (red line) allowing the variations in height to be more easily seen. For the smaller aspect ratios the deposits are the usual cone surrounded by a thin region of material (figure 4.3a). As the aspect ratio increases, however, a ridge appears (figure 4.3b) and grows with the aspect ratio. Around $a = 20$ (figure 4.3c) this reaches the same height as

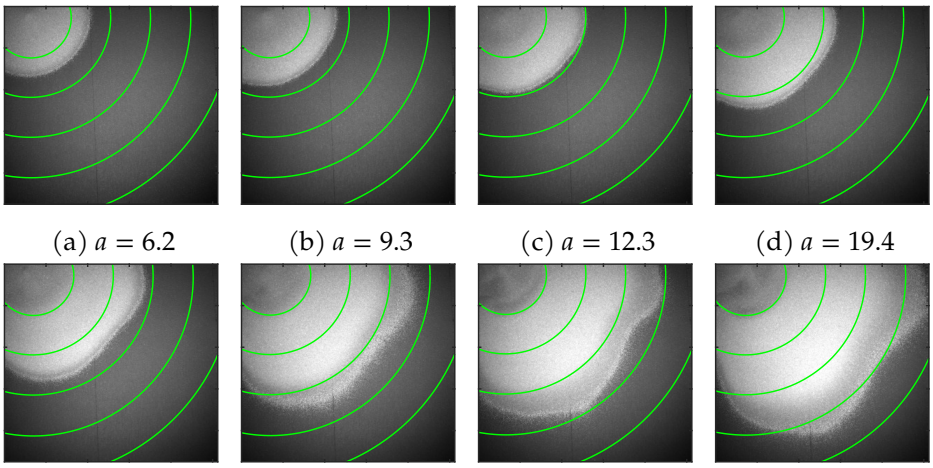

(a) $a = 6.2$ (b) $a = 9.3$ (c) $a = 12.3$ (d) $a = 19.4$

(e) $a = 26.0$ (f) $a = 33.0$ (g) $a = 39.1$ (h) $a = 46.3$

Figure 4.2: Final deposits for collapses of glass beads at varying aspect ratios. Green arcs are at 100 mm intervals.

the central cone and then exceeds it and becomes the highest part of the deposit.

More dramatically, however, the deposits become asymmetric at higher aspect ratios. This can be first seen around $a = 12$ (figure 4.2c) as a slight straightening of the deposit edge. As the aspect ratio increases the deposit becomes concave around $a = 33$ (figure 4.2f) and ultimately gives the final deposit a flower-like appearance (figure 4.2h).

Figures 4.4 and 4.5 show the variation in time of the raw video and radial velocities respectively along a radius along one of the deposit's petal-like lobes for each of the collapses. For low aspect ratios these time series are similar to the earlier collapses (compare, for example, figure 4.5a with figure 2.8e). Above $a \approx 10$ the flow front starts to slow at around 400 ms. Whilst this is initially a very small effect, it becomes bigger as the aspect ratio increases and is clearly visible in figure 4.4d. After a short period at

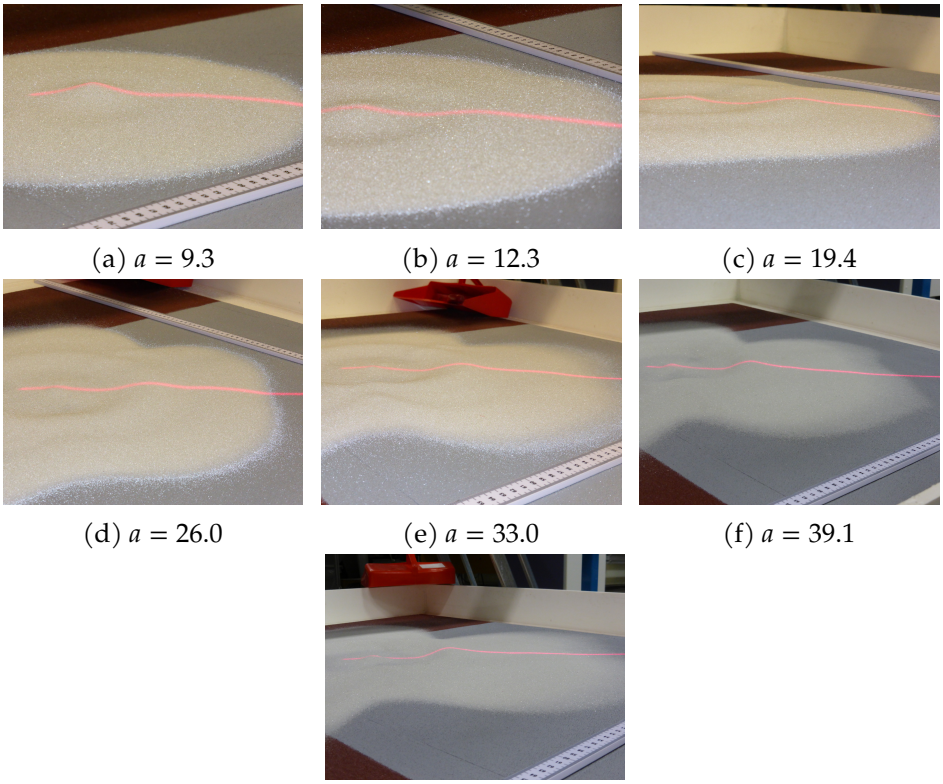

(a) $a = 9.3$ (b) $a = 12.3$ (c) $a = 19.4$

(d) $a = 26.0$ (e) $a = 33.0$ (f) $a = 39.1$

(g) $a = 46.3$

Figure 4.3: Side views of final deposits with vertically projected laser sheet (red line) to illustrate deposit profile. Collapses are the same as pictured in figure 4.2.

this slower speed, the flow front reaccelerates to its original speed.

As the aspect ratio is increased further the flow front accelerates again before slowing for a second time (figure 4.4e). For even higher aspect ratios this pattern repeats itself multiple times. The velocity time series in figure 4.5 show that each acceleration corresponds with a wave of fast moving material reaching and overrunning the deposit edge. Higher as-

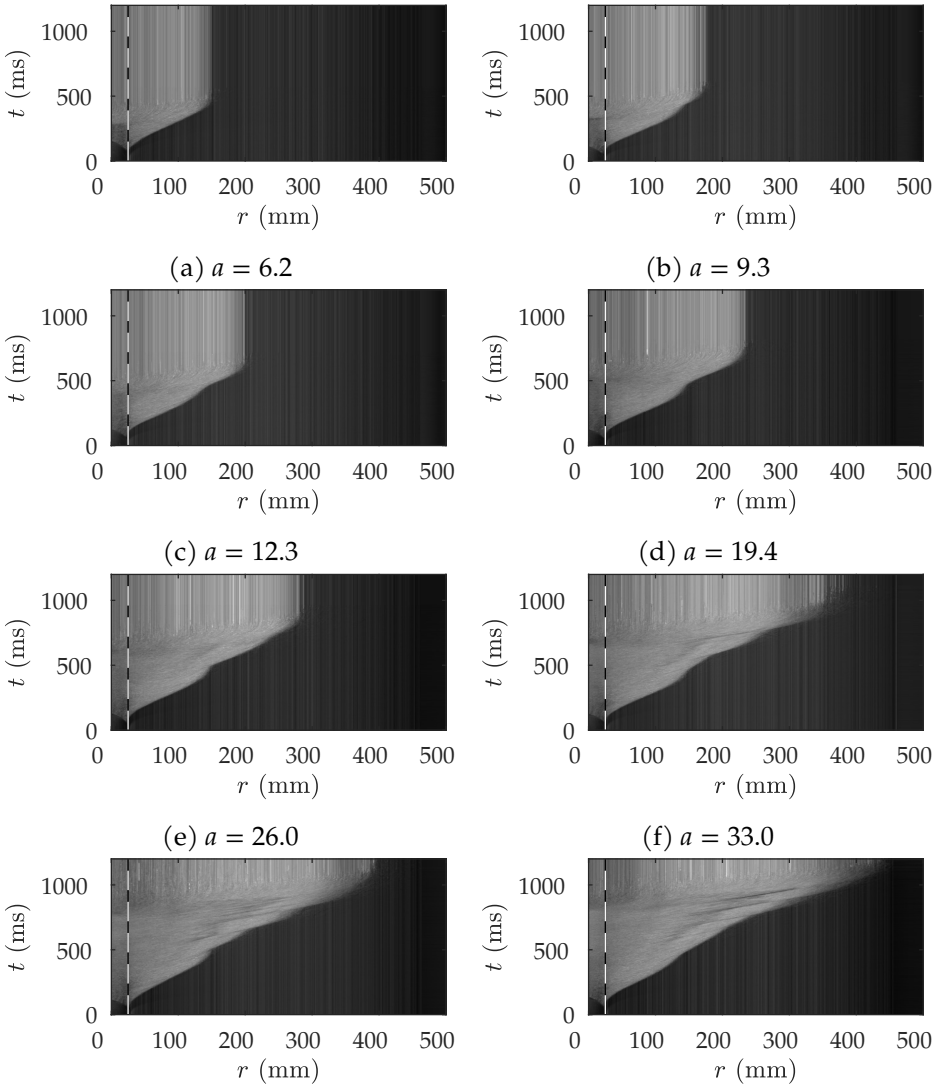

(a) $a = 6.2$ (b) $a = 9.3$

(c) $a = 12.3$ (d) $a = 19.4$

(e) $a = 26.0$ (f) $a = 33.0$

(g) $a = 39.1$ (h) $a = 46.3$

Figure 4.4: Video time series of very tall collapses of glass beads. The black and white line at 25 mm marks the initial radius of the column.

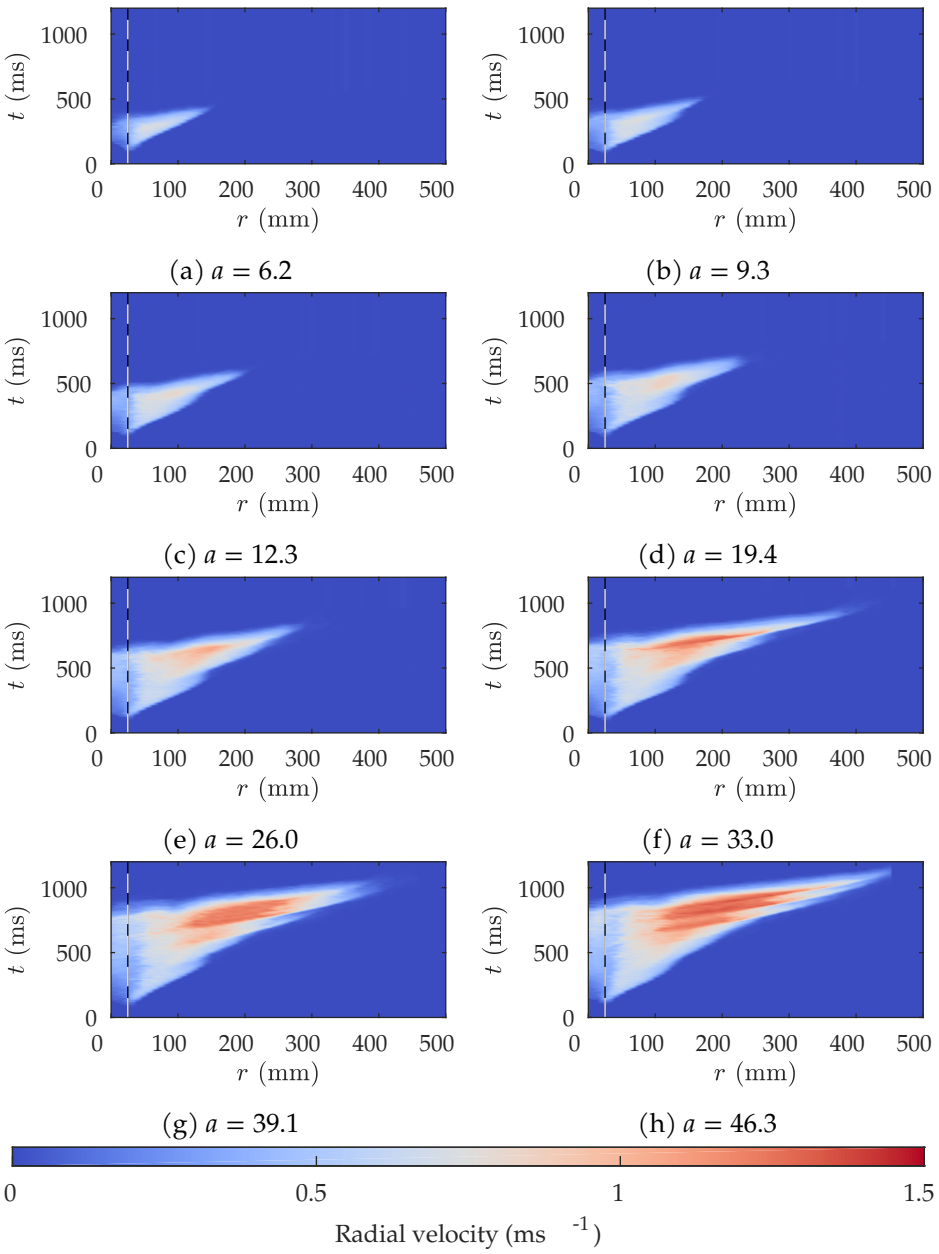

Figure 4.5: Radial velocity time series of very tall collapses of glass beads. The black and white line at 25 mm marks the initial radius of the column.

pect ratio collapses have more material and last longer, thereby allowing more waves to form.

Like with our earlier work at smaller aspect ratios, the different time series are very similar at early times. Once the waves begin to appear, however, there are differences in the time series for different aspect ratios. This suggests that the dynamics of the falling column become important at these higher aspect ratios.

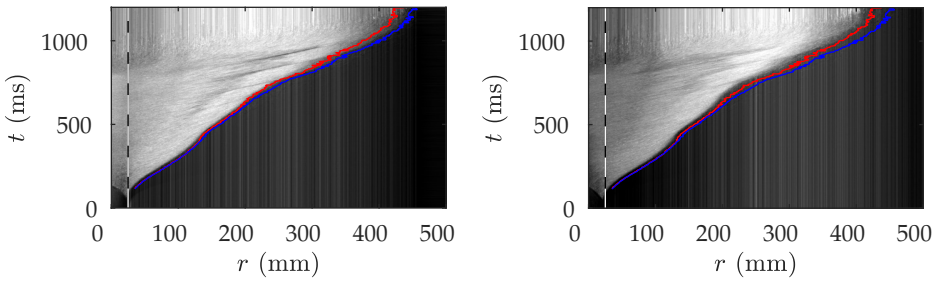

(a) Maximum extent

(b) Minimum extent

Figure 4.6: Comparison of the video time series along two different radii for a collapse of 3500 g of glass beads ($a = 46.3$). Coloured lines show the position of deposit edge at the points of minimum (red) and maximum (blue) extent. The black and white line at 25 mm marks the initial radius of the column.

Figures 4.6 and 4.7 compare the time series along two different radii for the largest collapse. Figures 4.6a and 4.7a are along the same radii as figure 4.5h, whereas figures 4.6b and 4.7b are taken along radii through the minimum extent of the deposit.

The time series along both radii are qualitatively very similar, with the same waves of material leading to the same accelerations and decelerations of the deposit edge occurring at the same times. The key difference occurs at around 350 ms where the deposit edge decelerates much more along the radius that will end up going through the point of minimum

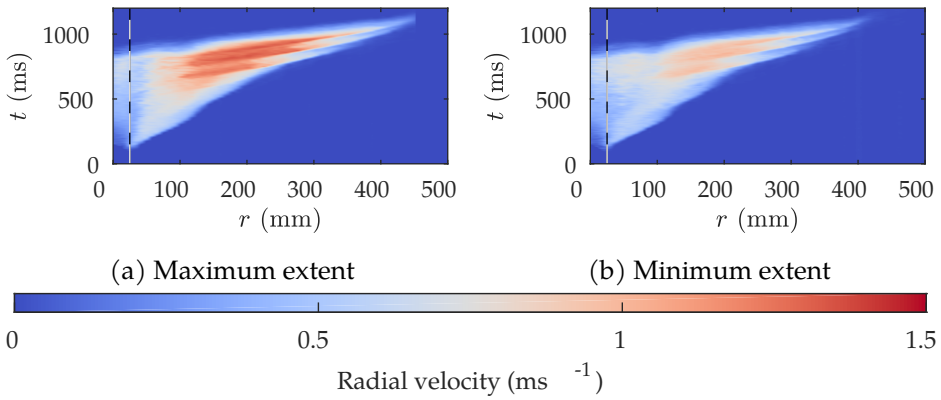

Figure 4.7: Comparison of the velocity time series for the same collapse and radii as in figure 4.6. The black and white line at 25 mm marks the initial radius of the column.

deposit extent. The flow then remains slower along this radius, resulting in the reduced run-out.

The progression of one of these waves can be seen in figure 4.8 with the fast moving material appearing darker than the rest of the flow. When the wave hits the edge of the deposit it exaggerates the previously existing asymmetry. This effect is repeated for each wave and is why the taller columns are so much more asymmetric than the shorter ones. In particular, there is no asymmetry for the lowest aspect ratio collapses that do not have a wave and little asymmetry for those where there is only one wave at the end of the collapse.

Another feature visible in these images is a region with a coarser texture than the rest of the flow. This is not present in the lower aspect ratio collapses (figure 2.4a). This is due to particles flowing up the ridge and becoming airborne as they pass the peak. The apparent texture is due to the shadows they cast on the bulk of the flow. Once these particles land they are indistinguishable from the rest and so the texture is not present

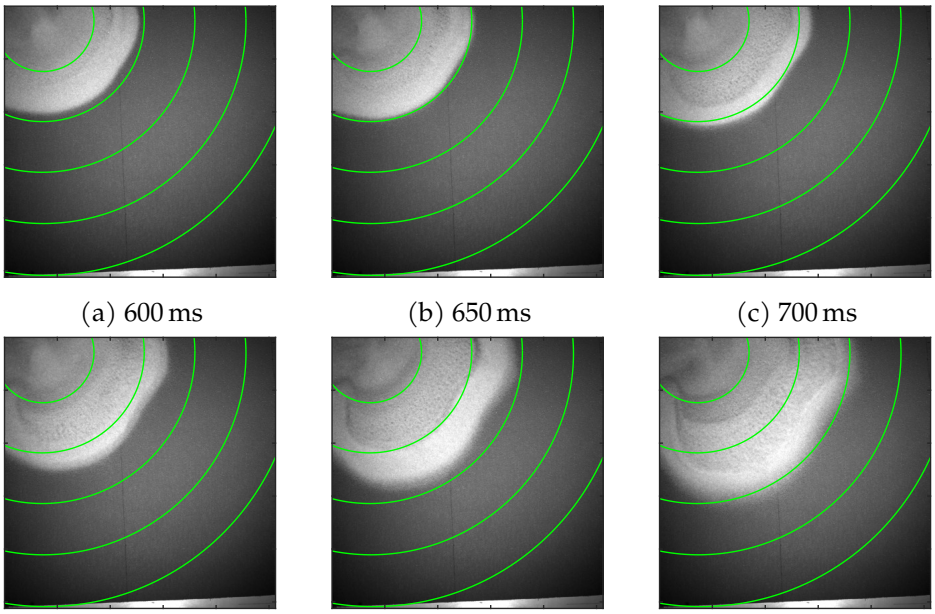

(a) 600 ms (b) 650 ms (c) 700 ms

(d) 750 ms (e) 800 ms (f) 850 ms

Figure 4.8: Snapshots from the video of the collapse of 3500 g of glass beads with an initial aspect ratio of 46.3. Green arcs are at 100 mm intervals.

in the final deposit (figure 4.2h).

Figure 4.9 shows the radial surface speeds for the same collapse and at the same times as in figure 4.8. We can clearly see how the faster moving material is in the regions that spread further and form the lobes of the final deposit.

Figure 4.10 shows photographs of the final deposits from three different collapses of the same mass of glass beads, all with initial aspect ratios of around 46. Figures 4.10b and 4.10c differ from figure 4.10a in that the tube used to hold the glass beads at the start of the experiment has been rotated by 90° and 180° about the vertical axis respectively. The result of

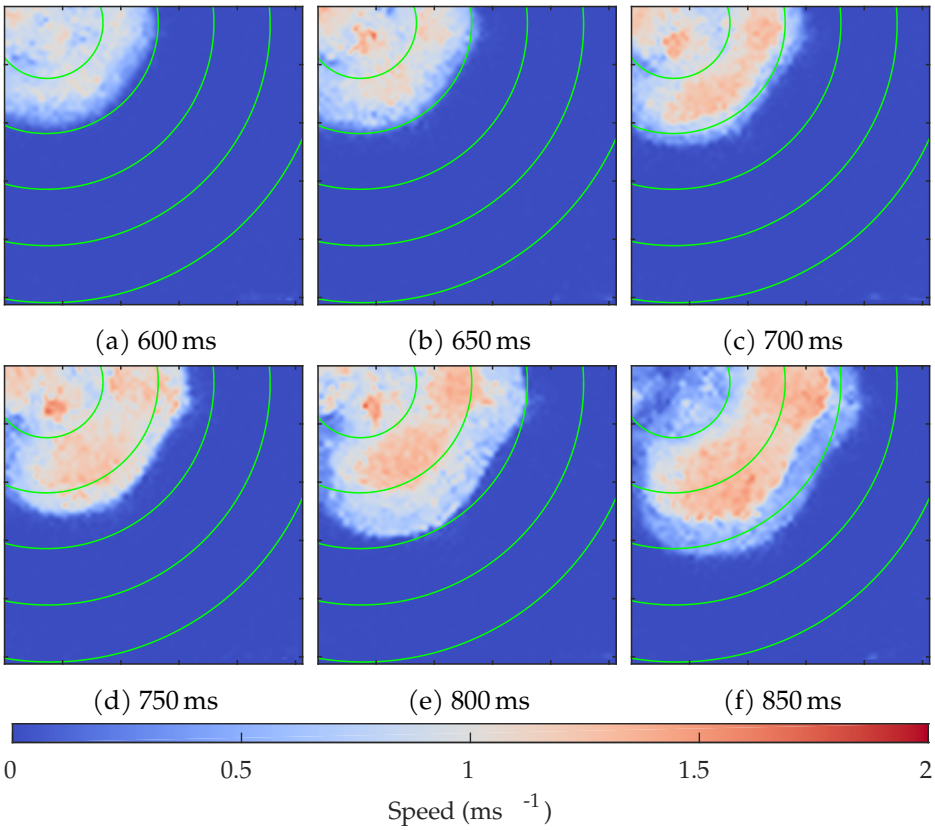

Figure 4.9: PIV calculated radial surface speeds for the collapse shown in figure 4.8. Green arcs are at 100 mm intervals.

this is a series of identically asymmetric deposits that are rotated by the same amount relative to each other. This shows that the asymmetries we have seen are set by the geometry of the tube rather than evolving during the flow.

This can be further seen in figure 4.10d which shows a collapse where the tube was flipped upside-down relative to figure 4.10a. Here we see a completely different asymmetry from before, again showing that the

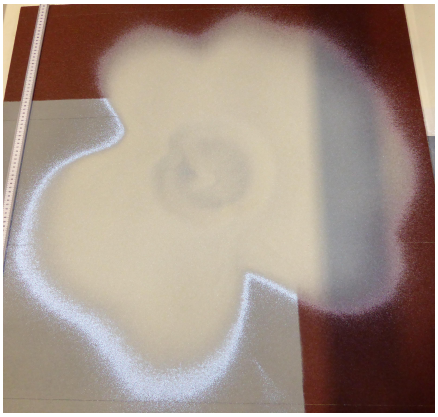

(a) Original orientation
($a = 46.3$)

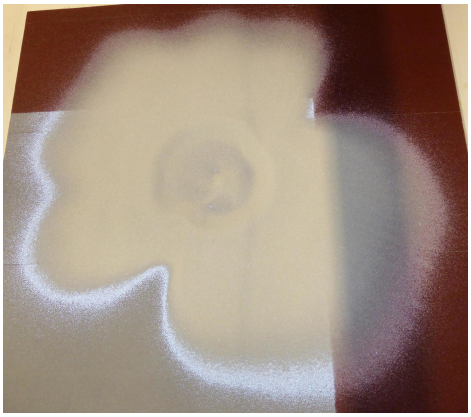

(b) Tube rotated by 90°
($a = 46.2$)

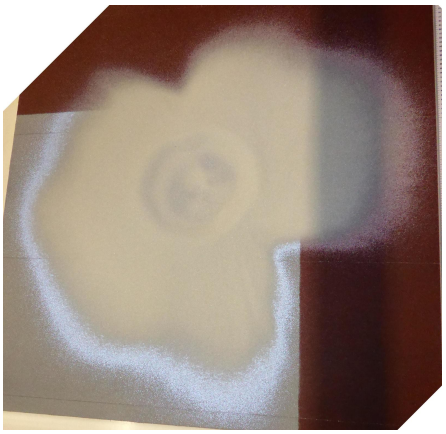

(c) Tube rotated by 180°
($a = 46.3$)

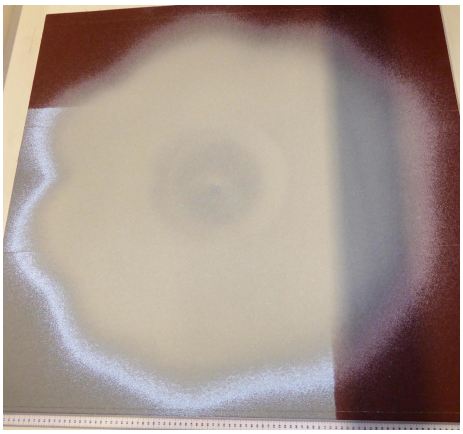

(d) Tube flipped vertically
($a = 45.8$)

Figure 4.10: Final deposits after four collapses of 3500 g of glass beads with varying orientations of tube.

asymmetry is due to the tube. This also demonstrates that the tube we used must be asymmetric along its length as well as just azimuthally.

Figure 4.11 shows a side view of a collapse of glass beads. From this

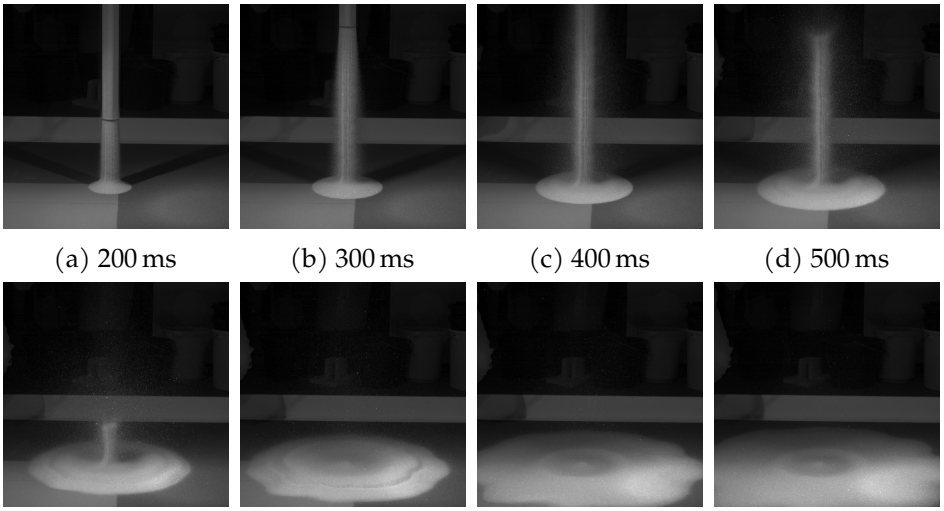

(a) 200 ms (b) 300 ms (c) 400 ms (d) 500 ms

(e) 600 ms (f) 700 ms (g) 800 ms (h) 900 ms

Figure 4.11: Side view of a collapse of 3197.2 g of glass beads with an initial aspect ratio of 43.0

view we can see the formation of the ridge at around 400 ms (figure 4.11c). As the flow continues, the ridge moves outwards and grows taller. When the column finishes falling, a final wave of material causes the ridge to shrink to its final height and position.

This also gives an alternative view of the formation of the instability. We first see signs of the deposit edge straightening at around 500 ms (figure 4.11d) but it is not until figure 4.11e that it is clearly visible. This matches with the slowing of the flow front discussed earlier. As time progresses the asymmetry becomes more distinct until the deposit edge flows out of frame and is no longer visible.

As before we see a differently textured region of material appear around 500 ms (figure 4.11d) and disappear by 800 ms (figure 4.11g). Again, this is from a series of waves of material flowing up and over the ridge and

becoming airborne. This process is clearest in the raw video but is less obvious in these still images.

This side view also allows us to see the falling column. Compared with the lower aspect ratio collapses (figure 3.4), we see far more expansion of the column as it leaves the cylinder. In addition, the falling column is surrounded by a region of individual particles that have sprayed out as the tube is lifted. These effects are likely caused by the extra weight of material in the initial column causing pressure on the sides of the cylinder. When the cylinder is retracted the particles are then free to expand outwards to give the observed behaviour.

We also see vertical streaks in the falling column. Whilst these could be purely an artefact of the lighting, the fact that they take time to appear (they are absent in figure 4.11a and only present in part of figure 4.11b) suggests that they are reflecting some physical feature of the column. In figures 4.11c and 4.11d there is a slight waviness to the streaks, possibly due to an instability in the features as the column falls. The verticality of the streaks suggests they are caused by the cylinder rather than from some instability in the fall. Although the evidence is unclear, figure 4.11e suggests that these streaks may line up with the asymmetries of the deposit.

A final feature is that the column appears to have some horizontal variations (clearest in figure 4.11d) rather than falling straight down like in the smaller collapses. The cause of this is unclear and may be due to vibrations of the cylinder and lifting apparatus or it could be a natural instability in the falling column (as in, e.g. Möbius (2006)). It is unclear what effect, if any, this has on the final deposit.

4.3.3 Sand

Another approach to investigating the asymmetries is to consider collapses of different granular materials. Choosing a material with a different coef-

ficient of friction has the potential to change the asymmetries observed.

As a first choice we used sand with similar sized grains to the glass beads we used previously (particle diameters roughly between 300 μm and 425 μm). These had a higher coefficient of friction than the glass beads. One immediate consequence was that the run-out distances were much shorter than with the glass beads and so we could perform collapses with the cylinder filled to its maximum height of 2000 mm ($a = 80$).

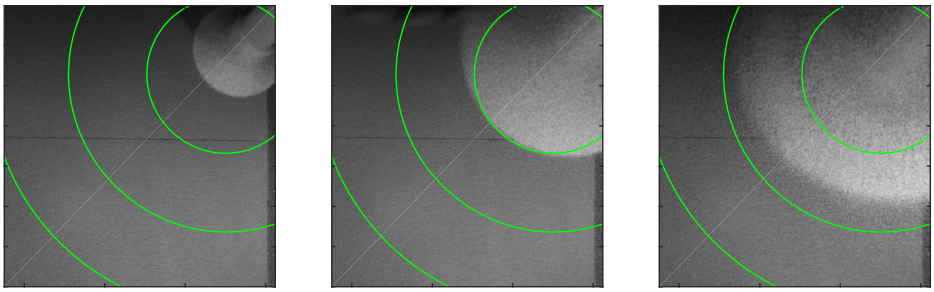

(a) 200 ms (b) 400 ms (c) 600 ms

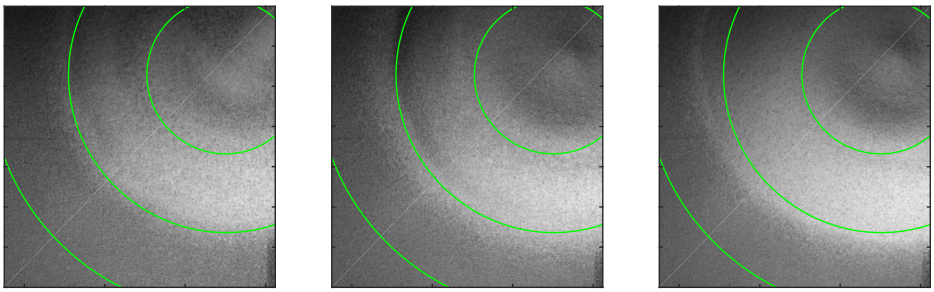

(d) 800 ms (e) 1000 ms (f) 1300 ms

Figure 4.12: Images from the collapse of a collapse of a column of 6067.1 g of sand. The column had an initial height of 2000 mm ($a = 80$). Green arcs are at 100 mm intervals.

Figure 4.12 shows the collapse of such a column of sand. Unlike with the glass beads, there is much less asymmetry in the deposit at all stages of the collapse. Despite being a much larger column in mass and initial

height, the run-out is significantly shorter than the collapses of glass beads described above. This is due to the much higher coefficient of friction of sand stopping the deposit before it expands as far. As a result the deposit is much thicker with a ridge that is taller than the typical central cone.

Like with the glass beads, we see coarsely textured regions in the flow (figures 4.12c and 4.12d). As before, we interpret this as particles flowing up the ridge and becoming airborne.

One new feature is that the speed of the deposit's expansion drops significantly long before the collapse finishes. Between 800 ms (figure 4.12d) and 1300 ms (figure 4.12f) there is relatively little change in deposit radius compared with the earlier times. This is due to the build up of the ridge stopping material from expanding outwards.

Figure 4.13 shows the surface radial speeds at each of the times in figure 4.12. The key feature here is the presence of a ring of slower material that can be seen in figures 4.13c and 4.13d. This corresponds to the inner edge of the outer ring and is due to material slowing down as it moves upwards. The upward motion is towards the camera and is, therefore, not picked up by the PIV algorithm, further reducing the measured speed.

This is further highlighted in the time series of figure 4.14. The inner edge of the ridge can be seen as a dark region in figure 4.14a, which clearly matches up with the slower moving region in figure 4.14b.

We can also clearly see how the deposit expansion significantly slows before the end of the collapse. This slowing begins at roughly 650 ms and there is very little expansion beyond around 800 ms. The presence of airborne particles confuses the image, making the deposit look larger than the actual bulk of the deposit.

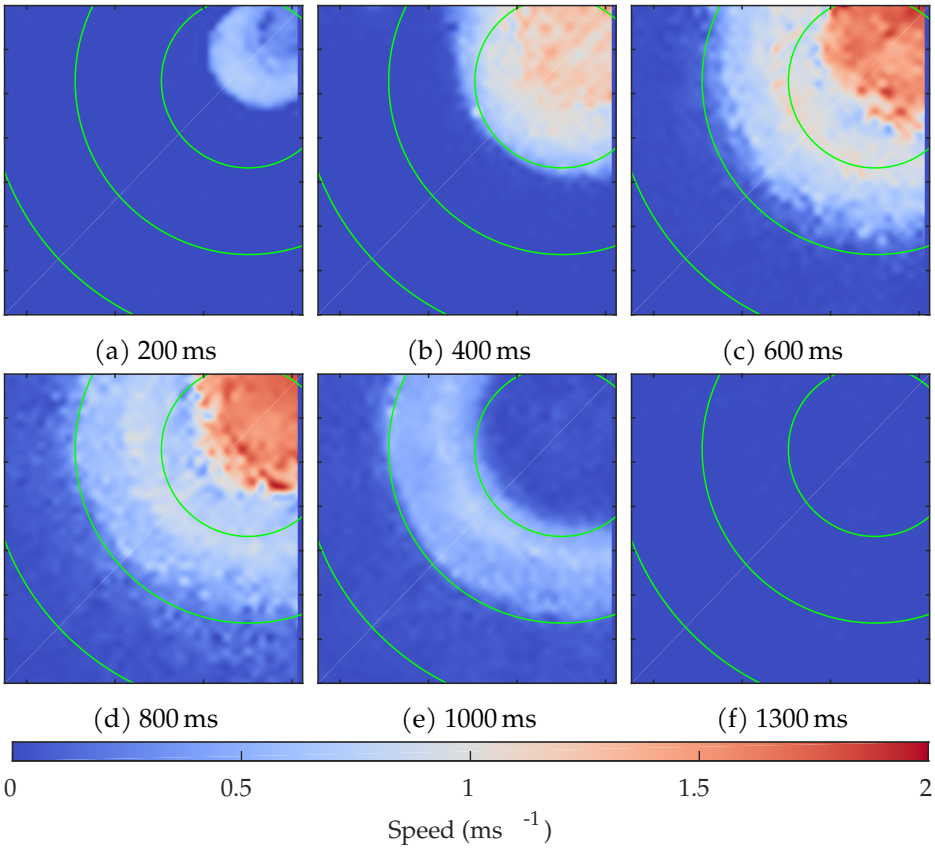

Figure 4.13: PIV calculated radial surface speeds for the collapse shown in figure 4.12. Green arcs are at 100 mm intervals.

4.3.4 Silicon carbide

We can further increase the coefficient of friction by using more angular silicon carbide grains as our material. Again we use particles with diameters roughly between 300 μm and 425 μm.

Figure 4.15 shows a series of images from the collapse of a column of silicon carbide with an initial aspect ratio of 80.72. Initially the collapse

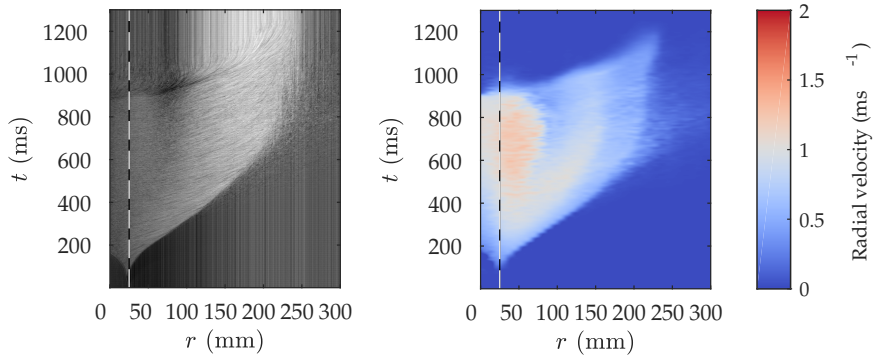

(a) Video data. (b) Radial velocity.

Figure 4.14: Time series for the collapse shown in figure 4.12. The black and white line at 25 mm marks the initial radius of the column.

spreads outwards as usual (figures 4.15a to 4.15c) but the expansion slows and eventually stops, leaving behind a ridge that can be seen in figure 4.15d. The column has not finished collapsing at this point and material builds up behind this ridge until it eventually avalanches an a wave of material rushes outwards (figures 4.15e and 4.15f). When this wave hits the ridge it is pushed upwards and becomes airborne (figures 4.15f to 4.15h) before landing in a thin, streaked region around a thicker central deposit (figure 4.15i).

The velocity data shown in figure 4.16 shows this more clearly. A region of fast moving material outside of the collapsing column can first be seen in figure 4.16d and the full ring can be clearly seen in figure 4.16e. In figure 4.16f this material reaches the deposit edge, matching the direct video observations.

The time series in figure 4.17 emphasise these features. In figure 4.17a we can clearly see the deposit stop expanding at around 650 ms like we saw with the sand collapse. The velocity time series in figure 4.17b shows the

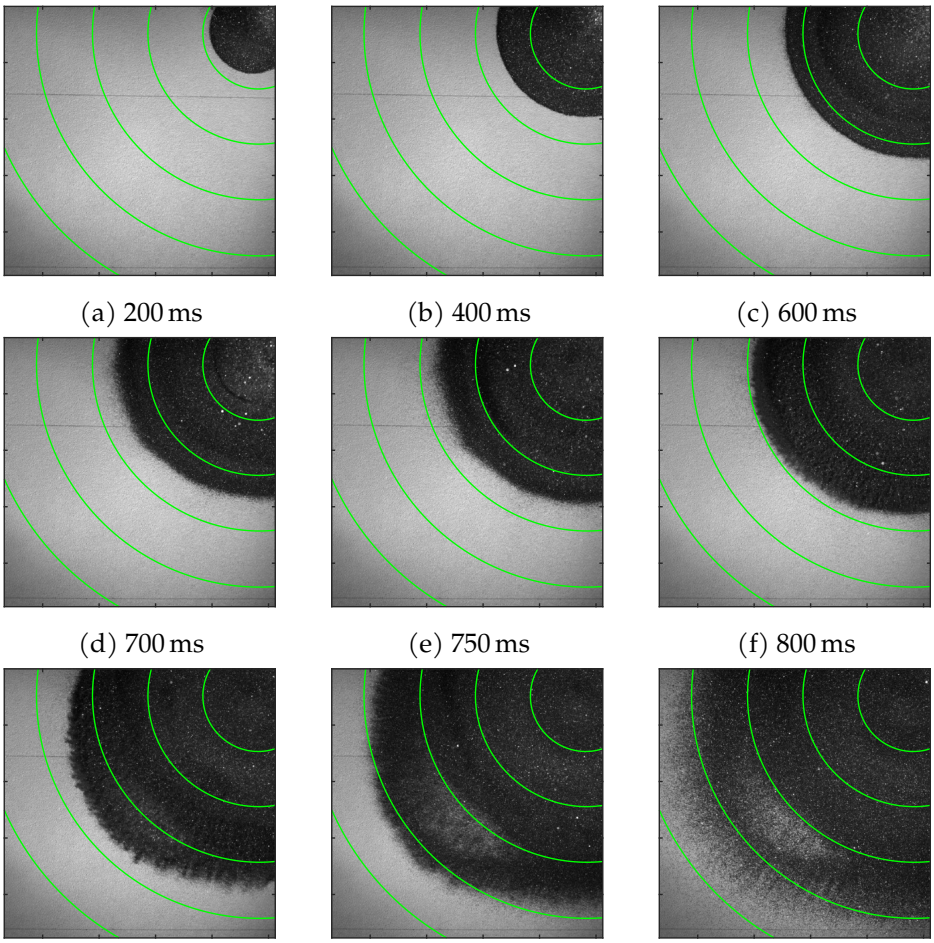

(a) 200 ms (b) 400 ms (c) 600 ms

(d) 700 ms (e) 750 ms (f) 800 ms

(g) 850 ms (h) 900 ms (i) 1100 ms

Figure 4.15: Images from the collapse of a collapse of a column of 5945.9 g of silicon carbide particles with diameters between 300 µm and 425 µm. The column had an initial height of 2018 mm ($a = 80.72$). Green arcs are at 100 mm intervals.

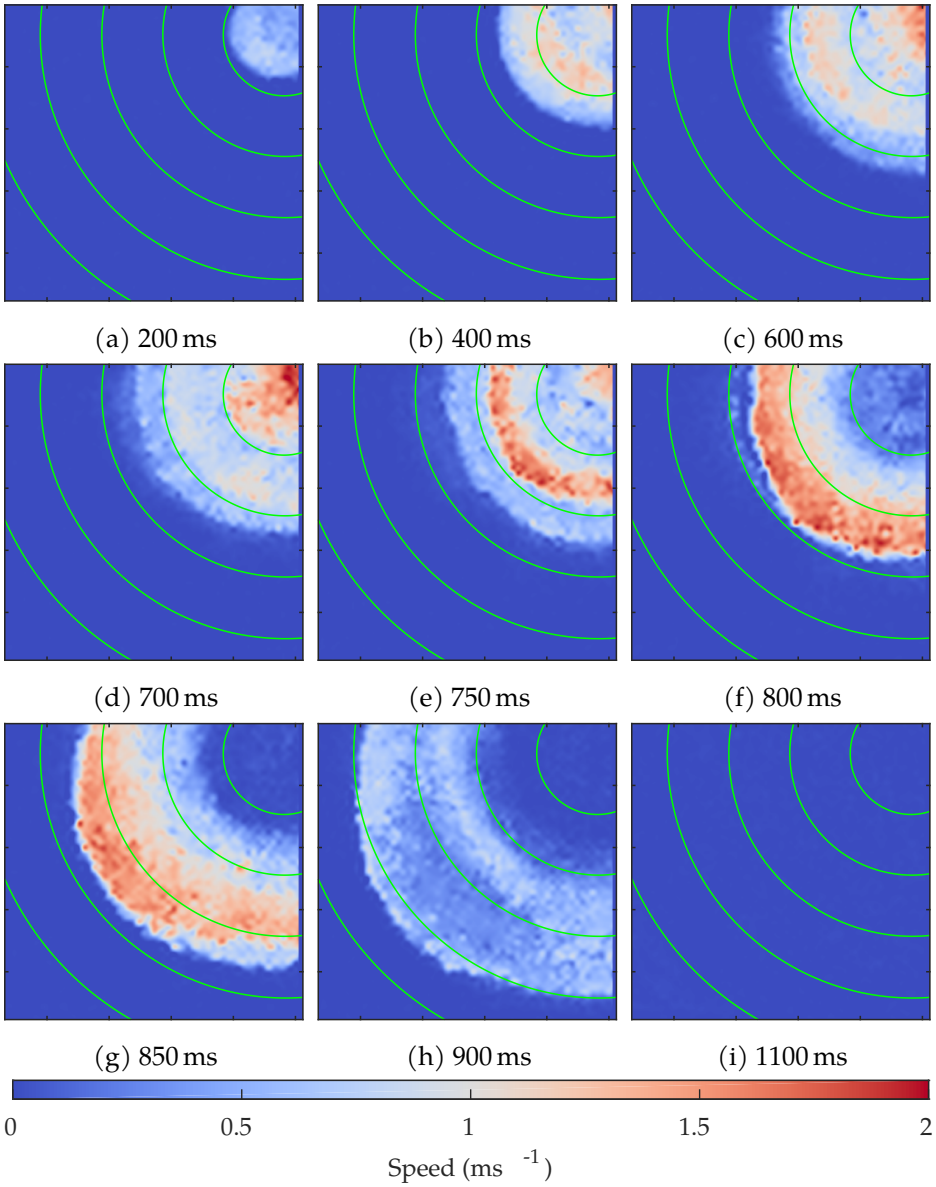

Figure 4.16: PIV calculated radial surface speeds for the collapse shown in figure 4.15. Green arcs are at 100 mm intervals.

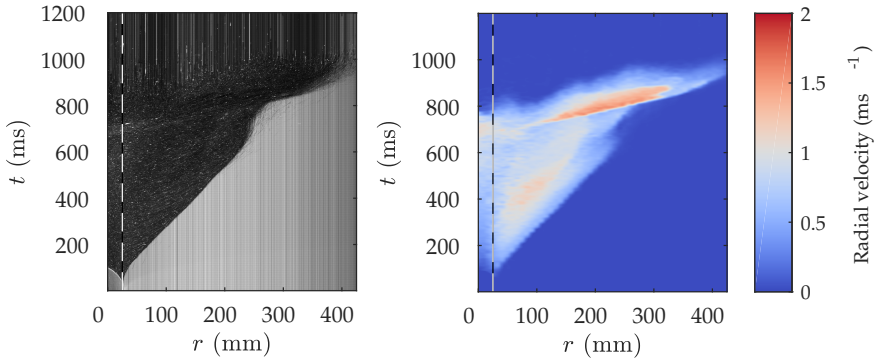

(a) Video data. (b) Radial velocity.

Figure 4.17: Time series for the collapse shown in figure 4.15. The black and white line at 25 mm marks the initial radius of the column.

fast moving ring forming and spreading outwards and over the deposit edge. The dramatic wave of airborne material can also be clearly seen to travel much faster than the initial spreading of the deposit.

4.4 Even higher aspect ratios

As the asymmetries we observed appeared to be due the cylinder, we replaced the original acrylic cylinder with an aluminium one. As these are manufactured differently, the aluminium cylinder was expected to be more symmetric than the previous cylinder, and so reduce or remove any cylinder induced asymmetries. At the same time we increased the cylinder length to 4 m to allow taller collapses to be considered, with the length ultimately being limited by the laboratory's height. The tube inner radius was also reduced slightly to 23.38 mm due to limitations in the sizes of tube that were commercially available and the need to keep the cylinder

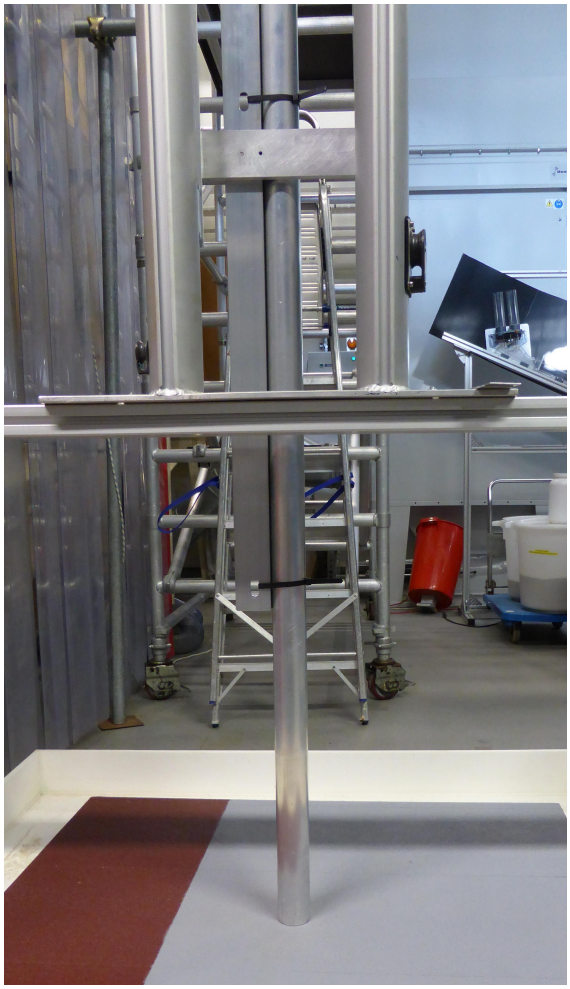

Figure 4.18: Photograph of the altered apparatus.

weight low enough to be manually lifted at speed. In addition, we extended the lifting carriage with the aim of reducing any vibrations that might cause asymmetries. This final apparatus can be seen in figure 4.18.

Figure 4.19 shows the final deposits from two different collapses of sand

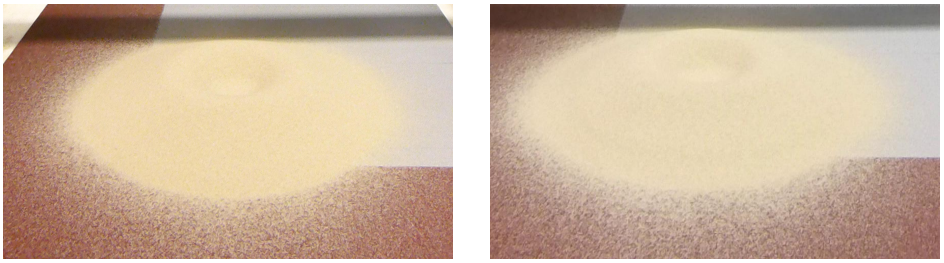

(a) Collapse of 11 428.0 g of sand. (b) Collapse of 11 330.7 g of sand.

Figure 4.19: Final deposits from two collapses with $a = 171$.

(glass beads would have run off the edge of the base) at the maximum possible aspect ratio of $a = 171$. Initially these were an attempt to consider the effect of packing fraction but the force of the falling sand in the filling process meant that we could not get differences of even 1%. Unlike previous collapses, the final deposit lacks a central cone and the ridge now forms the bulk of the deposit. The deposit can therefore be more naturally thought of as cratered cones. As a result the run-out distances were not significantly increased over the earlier sand collapses. The differences in deposit shape may be a result of how the sand leaves the cylinder.

Figure 4.20 shows a side view of various points in a typical collapse (specifically the collapse in figure 4.19a). Almost immediately a sideways oscillation appears in the flow (figure 4.20a), which persists as the collapse continues (figure 4.20b). Unlike with the first rig, the column does not fully leave the tube before the tube is pulled to its maximum height. In addition, friction between the sand and the tube results in a large amount of sand being lifted with the tube. When the tube reaches its maximum height, the remaining sand in the tube can flow out at a much faster rate than when it was being lifted. This sudden change in flow can be clearly seen in figure 4.20c.

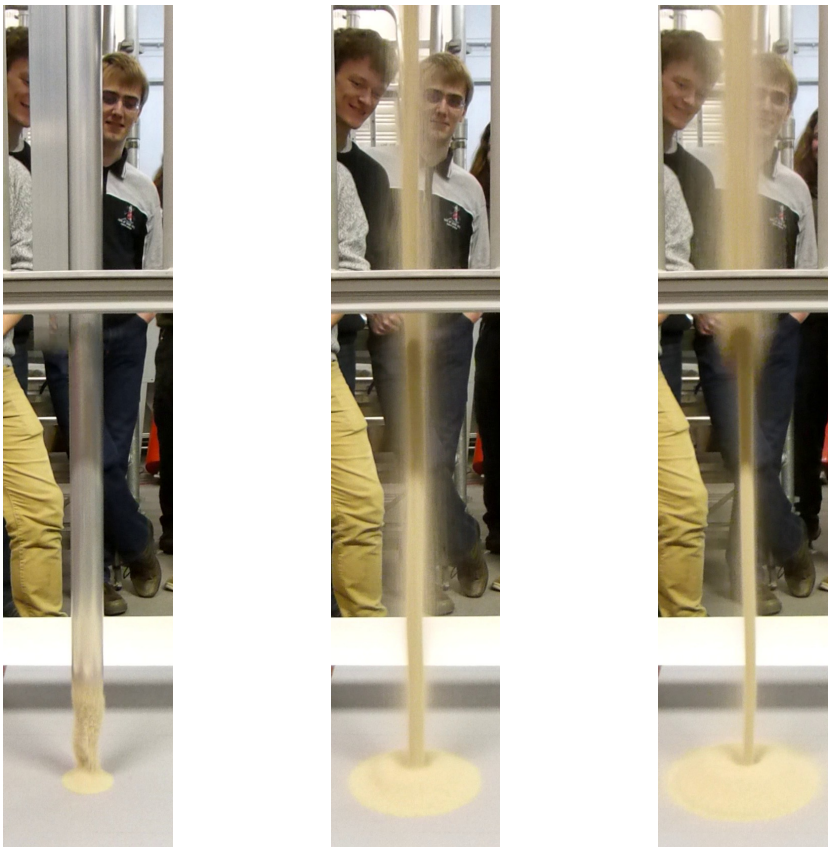

(a) 200 ms (b) 800 ms (c) 1300 ms

Figure 4.20: Images during the collapse of a column of 11 428.0 g of sand with an initial height of 4 m ($a = 171$).

4.5 Discussion

We have shown that, for all materials considered, the deposits from very tall column collapses are notably different from the shorter columns previously considered. As the aspect ratio increases, the central height begins to decrease whilst, away from the centre, a ridge forms and increases in height. A key characteristic of very tall column collapses is that this ridge eventually grows taller than the central peak to become the location of the deposit's maximum height. Whilst the ridge had been previously observed by Roche *et al.* (2011) they did not consider high enough aspect ratios for it to overtake the central peak in height.

This outer ridge also leads to particles becoming airborne as they pass over it. Whilst this effect is relatively small for the the collapses of glass beads and of sand, it leads to a sudden increase in deposit radius for the much rougher silicone carbide particles. This shows how particle type has a significant qualitative effect at very higher aspect ratios that has not been observed at lower ones.

Unlike in smaller collapses, we see asymmetries appearing in the final deposits. These appear to be triggered by asymmetries in the cylinder used to hold the material rather than a feature of the flow. This causes an asymmetric flow out of the cylinder and hence an asymmetric final deposit.

Whilst we did not observe any asymmetries with the second tube, the flow out of the tube was significantly different. Due to large amounts of material being lifted with the cylinder, the outflow varied over time in a manner unlike the smaller collapses. This means that the lifting process was no longer a good approximation of an instantaneous release, which may be the cause of the different deposit height profile. Using a wider or smoother cylinder would likely reduce the proportion of sand that was lifted. Reducing the tube lifting speed would reduce the amount of material

dragged upwards, but the smaller gap between the bottom of the tube and the base might have effects on the flow behaviour as it could restrict the rate at which the material could spread horizontally, particularly at early times.

One feature of both tube is that, unlike with the shorter columns, there is noticeable evolution of the falling column, as seen in figure 4.11. Other work (e.g. Möbius (2006)) has found that there are instabilities in a falling column of granular material, and these may be occurring in our experiments. The size of any instability would depend on how long the material has to fall meaning that they would be more prominent in taller columns where the material is falling for longer. They would also grow in influence towards the end of the collapse as later material falls for a greater period of time than earlier material.

5 Conclusions

5.1 Summary

Our most important finding is that, contrary to previous suggestions (e.g Lube *et al.*, 2004), the material used has a significant effect in the granular collapse problem. As described in section 2.3, even changing the particle diameter results in changes in the run-out distance and the final deposit height of otherwise identical set-ups. This is confirmed by our reanalysis of previous results in section 2.1.1. These differences become more pronounced as the initial aspect ratio, with the very tall columns considered in section 4.3 showing drastic qualitative differences between collapses of different materials. Our bidisperse results in section 3.4 show that combinations of materials have results intermediate of those of their constituent pure materials.

Like Roche *et al.* (2011), we observed a second change in the deposit shape with aspect beyond the previous studied transition around $a = 1$. As the aspect ratio increases the "Mexican hat" profile observed by Lajeunesse *et al.* (2004) develops a distinct circular ridge surrounding the central cone which shrinks in height. Eventually the ridge overtakes the cone as the highest part of the deposit.

The development of this ridge also changes the dynamics of the collapse process. As the ridge grows it slows the flowing material causing the deposit to stop expanding before the end of the collapse. Material builds up behind the ridge until it overflows as a fast moving wave. Collapses of

very tall columns are characterised by a series of these waves until the end of the collapse.

In addition we observed significant asymmetries in some of the very tall collapses that are likely due to asymmetries in the tube. These do not have a significant effect on the flow at smaller aspect ratios but become important once the ridge forms in the deposit. The small changes from the initial asymmetry are amplified by each wave of material preferentially flowing towards the regions that have spread the furthest. This is likely due to slight variations in flow out of the tube leading to azimuthal variations in the ridge's structure. The material then preferentially flows in the directions where the ridge provides the least resistance and results in a much larger asymmetry in the final deposit.

The bidisperse collapses did not exhibit significant amounts of segregation due to a lack of shearing across the interface between the particles. When segregation occurred it was limited to the very end of the collapse. Unstably stratified columns had slightly larger central heights and run-outs than stably stratified columns. The differences in run-out could be explained by the type of particle at the deposit edge and was not due to any differences in the flow dynamics.

5.2 Open questions

Despite our initial expectations, we observed little segregation in the bidisperse collapses. Using a more extreme particle size ratio would increase the rate of segregation to the point where it may be possible for it to occur during a collapse. Alternatively, performing very tall collapses with bidisperse materials would increase the time available for segregation to occur. Another option for further work would be to follow Caplan *et al.* (2014) and consider combinations of particles with different frictional prop-

erties. Their collapses were qualitatively different to those presented here but lack the more detailed analysis we have used.

The asymmetric deposits observed with the very tall collapses also deserve further attention. Whilst they clearly depend on the geometry of the initial column in a reproducible manner, it is unclear how that translates into the specific shapes observed. One simple approach would be to attach objects to the inside of a cylinder to see what effect they have on the flow and resultant deposits.

The differences due to the choice of material also deserve more study. Although we saw significant differences at very high aspect ratios, we did not perform experiments to find out at what aspect ratio these start to manifest.

The new behaviours we have observed in our experiments provide a test for numerical and analytic models for granular collapses. Our bidisperse collapses could be used to test whether segregation models can correctly demonstrate the lack of segregation that we observed. The extreme aspect ratios of the very tall collapses make DEM models infeasible and simple shallow-water-like models have already been shown to break down at much lower aspect ratios (Mangeney-Castelnau *et al.*, 2005). The presence of significant amounts of airborne particles during the tallest collapses is a challenge for many modelling approaches. The variations in behaviour between different particle types would also be a useful test of the applicability of models to different particles.

Bibliography

Balmforth, N. J. & Kerswell, R. R. 2005 Granular collapse in two dimensions. *Journal of Fluid Mechanics* **538**, 399–428.

Bridgwater, J. 2012 Mixing of powders and granular materials by mechanical means—A perspective. *Particuology* **10** (4), 397–427.

Caplan, J. S., Tunyasuvunakool, S., Dalziel, S. B. & Vriend, N. M. 2014 Segregation Effects in Granular Collapse. In *Geomechanics from Micro to Macro - Proceedings of the TC105 ISSMGE International Symposium on Geomechanics from Micro to Macro, IS-Cambridge 2014* (ed. Matthew Kuo Kenichi Soga, Krishna Kumar, Giovanna Biscontin), pp. 1559–1563. Taylor and Francis - Balkema.

Chen, W., Qiu, T. & Asce, M. 2012 Numerical Simulations for Large Deformation of Granular Materials Using Smoothed Particle Hydrodynamics Method. *International Journal of Geomechanics* **12** (2), 127–135.

Crosta, G. B., Imposimato, S. & Roddeman, D. 2009 Numerical modeling of 2-D granular step collapse on erodible and nonerodible surface. *Journal of Geophysical Research* **114** (F3), F03020.

Dalziel, S. B. 2006 Digiflow user guide. *www.damtp.cam.ac.uk/lab/digiflow/* .

Dalziel, S. B., Hughes, G. O. & Sutherland, B. R. 2000 Whole-field density measurements by 'synthetic schlieren'. *Experiments in Fluids* **28** (4), 322–335.

Degaetano, M., Lacaze, L. & Phillips, J. C. 2013 The influence of localised size reorganisation on short-duration bidispersed granular flows. *European Physical Journal E* **36** (4), 1–9.

Doyle, E. E., Huppert, H. E., Lube, G., Mader, H. M. & Sparks, R. S. J. 2007 Static and flowing regions in granular collapses down channels: Insights from a sedimenting shallow water model. *Physics of Fluids* **19** (10), 106601.

Drahun, J. A. & Bridgwater, J. 1983 The mechanisms of free surface segregation. *Powder technology* **36** (1983), 39–53.

GDR MiDi 2004 On dense granular flows. *The European physical journal. E, Soft matter* **14** (4), 341–365.

Hogg, A. J. 2007 Two-dimensional granular slumps down slopes. *Physics of Fluids* **19** (9), 093301.

Jop, P., Forterre, Y. & Pouliquen, O. 2005 Crucial role of sidewalls in granular surface flows: consequences for the rheology. *Journal of Fluid Mechanics* **541**, 167–192.

Jop, P., Forterre, Y. & Pouliquen, O. 2006 A constitutive law for dense granular flows. *Nature* **441** (7094), 727–30.

Kerswell, R. R. 2005 Dam break with Coulomb friction: A model for granular slumping? *Physics of Fluids* **17** (5), 057101.

Lacaze, L. & Kerswell, R. R. 2009 Axisymmetric Granular Collapse: A Transient 3D Flow Test of Viscoplasticity. *Physical Review Letters* **102** (10), 108305.

Lagrée, P.-Y., Staron, L. & Popinet, S. 2011 The granular column collapse as a continuum: validity of a two-dimensional Navier-Stokes model with a μ(I)-rheology. *Journal of Fluid Mechanics* **686**, 378–408.

Lajeunesse, E., Mangeney-Castelnau, A. & Vilotte, J. P. 2004 Spreading of a granular mass on a horizontal plane. *Physics of Fluids* **16** (7), 2371.

Lajeunesse, E., Monnier, J. B. & Homsy, G. M. 2005 Granular slumping on a horizontal surface. *Physics of Fluids* **17** (10), 103302.

Larrieu, E., Staron, L. & Hinch, E. J. 2006 Raining into shallow water as a description of the collapse of a column of grains. *Journal of Fluid Mechanics* **554**, 259–270.

Lube, G., Huppert, H. E., Sparks, R. S. J. & Freundt, A. 2005 Collapses of two-dimensional granular columns. *Physical Review E* **72** (4), 41301.

Lube, G., Huppert, H. E., Sparks, R. S. J. & Hallworth, M. A. 2004 Axisymmetric collapses of granular columns. *Journal of Fluid Mechanics* **508**, 175–199.

Mangeney, A., Staron, L., Volfson, D. & Tsimring, L. 2007 Comparison between discrete and continuum modeling of granular spreading. *WSEAS Transactions on Mathematics* **6** (2), 373–380.

Mangeney-Castelnau, A., Bouchut, F., Vilotte, J. P., Lajeunesse, E., Aubertin, A. & Pirulli, M. 2005 On the use of Saint Venant equations to simulate the spreading of a granular mass. *Journal of Geophysical Research B: Solid Earth* **110** (9), 1–17.

Mast, C. M., Arduino, P., Mackenzie-Helnwein, P. & Miller, G. R. 2014 Simulating granular column collapse using the Material Point Method. *Acta Geotechnica* .

Meruane, C., Tamburrino, A. & Roche, O. 2010 On the role of the ambient fluid on gravitational granular flow dynamics. *Journal of Fluid Mechanics* **648**, 381–404.

Möbius, M. E. 2006 Clustering instability in a freely falling granular jet. *Physical Review E* **74** (5), 051304.

Phillips, J. C., Hogg, A. J., Kerswell, R. R. & Thomas, N. 2006 Enhanced mobility of granular mixtures of fine and coarse particles. *Earth and Planetary Science Letters* **246** (3-4), 466–480.

Pouliquen, O., Delour, J. & Savage, S. B. 1997 Fingering in granular flows. *Nature* **386** (6627), 816–817.

Pouliquen, O. & Vallance, J. W. 1999 Segregation induced instabilities of granular fronts. *Chaos (Woodbury, N.Y.)* **9** (3), 621–630.

Riber, S. 2017 Numerical methods for the simulation of continuum granular flow models. PhD thesis, MINES ParisTech.

Roche, O., Attali, M., Mangeney, A. & Lucas, A. 2011 On the run-out distance of geophysical gravitational flows: Insight from fluidized granular collapse experiments. *Earth and Planetary Science Letters* **311** (3-4), 375–385.

Roche, O., Gilbertson, M. A., Phillips, J. C. & Sparks, R. S. J. 2005 Inviscid behaviour of fines-rich pyroclastic flows inferred from experiments on gas-particle mixtures. *Earth and Planetary Science Letters* **240** (2), 401–414.

Savage, S. B. & Hutter, K. 1989 The motion of a finite mass of granular material down a rough incline. *Journal of Fluid Mechanics* **199** (-1), 177.

Siavoshi, S. & Kudrolli, A. 2005 Failure of a granular step. *Physical Review E* **71** (5), 051302.

Staron, L. & Hinch, E. J. 2005 Study of the collapse of granular columns using two-dimensional discrete-grain simulation. *Journal of Fluid Mechanics* **545**, 1–27.

Staron, L. & Hinch, E. J. 2006 The spreading of a granular mass: role of grain properties and initial conditions. *Granular Matter* **9** (3-4), 205–217.

Trepanier, M. & Franklin, S. 2010 Column collapse of granular rods. *Physical Review E* **82** (1), 11308.

Warnett, J. M. 2014 Stationary and rotational axisymmetric granular column collapse. PhD thesis, University of Warwick.

Warnett, J. M., Denissenko, P., Thomas, P. J., Kiraci, E. & Williams, M. A. 2013 Scalings of axisymmetric granular column collapse. *Granular Matter* **16** (1), 115–124.

Zenit, R. 2005 Computer simulations of the collapse of a granular column. *Physics of Fluids* **17** (3), 031703.